INSTITUTE OF NATURAL AND APPLIED SCIENCES

UNIVERSITY OF ÇUKUROVA

MASTER THESIS

Suzan BAŞEĞMEZ

CMS-CASTOR FORWARD DETECTOR AND 2007 TEST BEAM DATA ANALYSIS

DEPARTMENT OF PHYSICS

ADANA, 2008

THE INSTUTUTE OF NATURAL AND APPLIED SCIENCE
ÇUKUROVA UNIVERSITY

CMS-CASTOR FORWARD DETECTOR AND 2007 TEST BEAM DATA ANALYSIS

By Suzan BAŞEĞMEZ
A THESIS OF MASTER OF SCIENCE
DEPARTMENT OF PHYSICS

We certify that the thesis titled above was reviewed and approved for the award of degree of Master of Science by board of jury on ..../…....../ 2008 .

Signature.................   Signature.................   Signature..................

Prof.Dr. Gülsen ÖNENGÜT   **Assoc.Prof.Dr.Aysel KAYIŞ**   **Assist. Prof. Dr. Nuri**
SUPERVISOR   **TOPAKSU**   **EMRAHOĞLU**
        MEMBER   **MEMBER**

This MSc Thesis is performed in the Physics Department of the Institute of Natural and Applied Science of Çukurova University.

Registration Number:

Prof. Dr. Aziz ERTUNÇ
Director
The Institute of Natural
and Applied Science
Signature and Seal

ABSTRACT

MSc THESIS

CMS-CASTOR FORWARD DETECTOR AND 2007 TEST BEAM DATA ANALYSIS

Suzan BAŞEĞMEZ

DEPARTMENT OF PHYSICS
INSTITUTE OF NATURAL AND APPLIED SCIENCES
UNIVERSITY OF ÇUKUROVA

CASTOR is a Cherenkov sampling calorimeter, to be installed as a sub-detector of the CMS Experiment at the LHC. It will be positioned in the very forward region, 14.38 m away from the interaction point and covering the pseudo rapidity range $5.1 < |h| < 6.6$. In order to test the final design of the CASTOR calorimeter, a beam test in 2007 was carried out in the CERN/SPS H2 beam line for prototype III which consisted of successive layers of tungsten and quartz plates. The calorimeter prototype was exposed to various energies of muons, pions and electrons during the tests. In this thesis, after an overview of calorimetry, the physics and the final design of the CASTOR, we present the results of the electromagnetic response linearity and resolution of the calorimeter prototype, as well as leakage and beam contamination studies.

KeyWords: LHC, CMS, CASTOR, Calorimeter, Centauro, Strangelets

ÖZ

YÜKSEK LİSANS

CMS DENEYİNDE, İLERİ KALORİMETRE OLARAK KULLANILACAK OLAN CASTOR KALORİMETRESİNİN 2007 HÜZME TESTİ ANALİZİ

Suzan BAŞEĞMEZ

ÇUKUROVA ÜNİVERSİTESİ
FEN BİLİMLERİ ENSTİTÜSÜ
FİZİK ANABİLİM DALI

Danışman: Prof. Dr. Gülsen ÖNENGÜT

Yıl: 2008   Sayfa: 76

Jüri: Prof. Dr. Gülsen ÖNENGÜT
        Doç. Dr. Aysel KAYIŞ TOPAKSU
        Yrd. Doç. Dr. Nuri EMRAHOĞLU

CASTOR, BHÇ deki CMS deneyine yerşeştirilecek olan bir Çerenkov örnekleme kalorimetresidir. Çarpışma noktasındadan 14,38 m uzağa $5,1 < |h| < 6,6$ pseudorapidite bölgesini kaplayacak şekilde yerleştirilecektir. CASTOR için dizayn edilmiş olan prototip III, tungsten ve kuvartz plakalardan oluşmuştur. CASTOR kalorimetresinin prototip III için hüzme testleri CERN/SPS H2 deney alanında 2007 yılında gerçekleştirilmiştir. Kalorimetre prototipi çeşitli enerjilerdeki müon, pion ve elektronlarla test edilmiştir. Bu tezde, kalorimetrik yöntemler, araştırılacak fizik konuları ve CASTOR için kararlaştırılan son dizayn gözden geçirildikten sonra, elektomanyetik sızıntı ve hüzme kirliliği çalışmalarıyla, kalorimetre prototipinin elektromanyetik doğrusallığı ve çözünürlüğü sunulmaktadır.

Anahtar Kelimeler: CMS, CASTOR, BHÇ, Kalorimetre, Centauro, Strangelets

ACKNOWLEDGEMENTS

CONTENTS **PAGE**

LIST OF SYMBOLS AND ABBREVIATIONS

SM   **:** Standard Model

BSM   **:** Beyond Standard Model

LHC   **:** Large Hadron Collider

CMS   **:** Compact Muon Solenoid

**CASTOR : ** Centauro and Strange Object Research Detector

CERN   **:** European Nuclear Research Laboratory

QCD   **:** Quantum Chromo Dynamics

QGP   **:** Quark Gluon Plasma

SQM   **:** Strange Quark Matter

QM   **:** Quark Matter

EM   **:** Electromagnetic Channel

HAD   **:** Hadronic Channel

SU   **:** Sampling Unit

RU   **:** Readout Unit

MeV   **:** Million Electron Volt

GeV   **:** Giga Electron Volt

TeV   **:** Billion Electron Volt

PS   **:** Proton Synchrotron

SPS   **:** Super Proton Synchrotron

P_T **:** Transverse Momentum

E_T **:** Transverse Energy

Λ   **:** Interaction Length

X_0 **:** Radiation Length

A   **:** Atomic Number

LIST OF TABLES   **PAGE**

XIII

1. INTRODUCTION

The goal of High Energy Physics is to answer these questions: what are the fundamental constituents of matter and what are the fundamental forces controlling the behavior of matter? In order to answer these questions, we need to identify the intrinsic features and characteristics of particles at the basic level. For this, we need to employ well-defined devices to prove physical models. The LHC (Large Hadron Collider) at CERN (European Nuclear Research Laboratory) is the largest accelerator in the world where different detectors will operate. It is constructed to provide opportunities in High Energy Particle Physics, offering an unprecedented center of mass energy of 14 TeV and 5.5 TeV for proton-proton and lead-lead collisions, respectively, and luminosities up to 10^{34} cm^{-2}s^{-1} (10^{27} cm^{-2}s^{-1} for Pb-Pb collisions).

CMS (Compact Muon Solenoid) is one of the detectors which will be operating at the LHC. The principal aim of the CMS experiment is the discovery of the Higgs boson. In addition to the search for Higgs, a broad physics program will be covered, including the heavy-ion physics subjects. One of the goals of the CMS experiment is also to provide evidence of Super Symmetry (SUSY) beyond SM (Standard Model) in proton-proton collisions and to study Quantum Chromo Dynamics (QCD) in extreme conditions of temperature and density produced in Pb-Pb collisions.

The CMS detector consists of a silicon tracker, an electromagnetic calorimeter and a hadron calorimeter, surrounded by a high field superconducting solenoid. Together with muon detectors, as well as forward sampling calorimeters, it covers most of the 4π solid angle and a wide pseudorapidity range. The CASTOR (Centauro and Strange Object Research) calorimeter is one of the forward detectors of CMS which is dedicated to the search of Centauro-type events in heavy-ion collisions, related to previous exotic cosmic ray phenomena which have been studied in many experiments.

In order to test the performance of the CASTOR calorimeter before installation to the CMS, several prototypes (Prototype I and II) have been tested with beams at the CERN/SPS H2 beam line. This thesis presents the general and technical

features of CASTOR Prototype III and the data analysis for electromagnetic part of the prototype, tested with different configurations. In section 2, we introduce CASTOR calorimeter discussing the physics topics which will be researched with it. Then the calorimetric methods and basic features of calorimeters are presented in section 3. After giving the information and results from previous beam tests for prototype I and prototype II, we describe in details the engineering and mechanical construction of CASTOR Prototype III in section 4. Subsequently, the performance studies of the electromagnetic part including energy response linearity and resolution studies of CASTOR Prototype III are presented. In addition to these, different event cuts and beam contamination studies as well as the leakage studies are discussed in the same section. As a conclusion, in the last section, the analysis results from the beam test 2007 for CASTOR Prototype III are discussed.

2. PREVIOUS RESULTS

2.1. CASTOR Forward Detector of CMS Experiment

The CASTOR detector is a Cherenkov based quartz-tungsten sampling calorimeter which has been proposed to study the very forward rapidity (baryon-rich) region in heavy ion collisions in the multi-TeV range at the LHC and thus to complement the heavy ion physics programme, focused mainly in the baryon-free mid rapidity region (CASTOR EDR, 2007).CASTOR will be installed in the CMS experiment at 14.38 m from the interaction point, covering the pseudo rapidity range $5.1 < \eta < 6.6$. Thus, the calorimeter will contribute not only to the heavy ion program, but also to diffractive and low-x QCD physics in p-p collisions.

The CASTOR calorimeter is an electromagnetic (EM) and hadronic (HAD) detector, 16-fold azimuthally symmetric around the beam pipe. It is also longitudinally segmented into 14 sections, 2 for the EM and 12 for the HAD parts. Figure 2.1 shows the schematic design of the calorimeter. The calorimeter is constructed in layers of tungsten (W) plates as absorber and fused silica quartz (Q) plates as active medium. The signal is the Cherenkov light produced by the passage of the charged particles through the quartz medium. These W/Q-layers are inclined at $45^{\,o}$ to the beam direction, in order to maximize the Cherenkov light output.
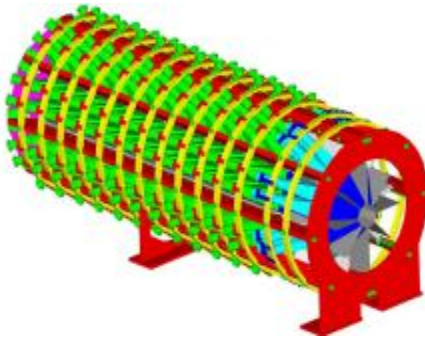
Figure 2.1. Schematic design of the full CASTOR calorimeter simulated with MC
            (Panagiotou, 2007)

Some basic properties of the active material are (CASTOR EDR, 2007):

-The index of refraction of quartz plate is $n = 1.46$-1.55

-Wavelengths $\lambda = 600$-200 nm.

-Cherenkov threshold velocity is $\beta_c = 1/n = 0.65$-0.69

-The angle of emission is $\theta_c = \arc \cos(1/n\beta) = 46^{\circ}$-$50^{\circ}$.

The calorimeter has 16×14 subdivisions and 224 channels in total. The light produced in each one is collected and focused by air-core light guides onto the corresponding PMTs. There are 5 tungsten/quartz layers, "Sampling Units" (SU), per subdivision, each read by a Reading Unit (RU), in both the EM and HAD sections (see CASTOR EDR, 2007). This calorimeter design and components can be clearly seen in Figure 2.2.
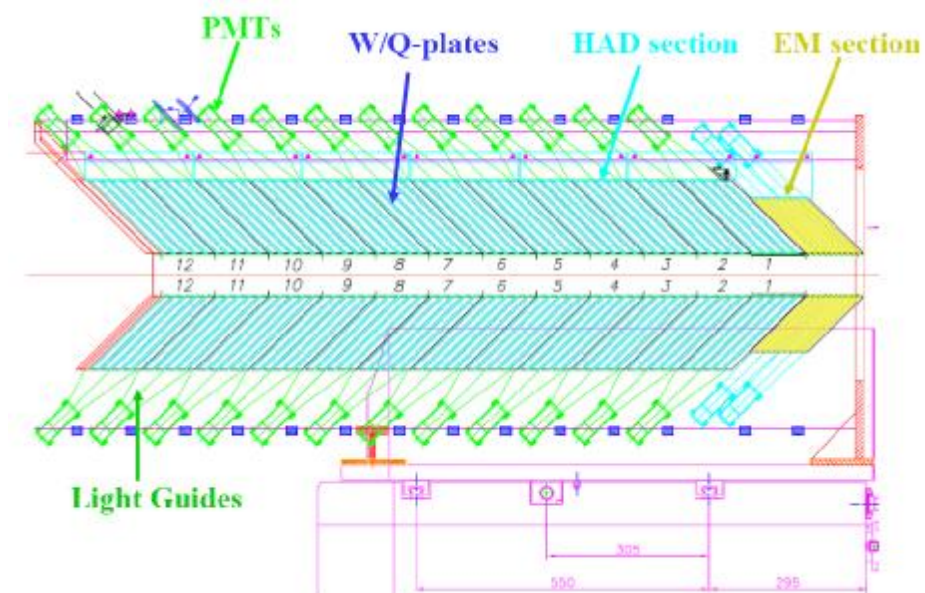
Figure 2.2. Schematic longitudinal view of the CASTOR Calorimeter design
        (Panagiotou, 2007)

Figure 2.3 shows the front view of the calorimeter design, with the four octants forming half of the calorimeter. The subdivision of each octant into two semi-octants (8-fold segmentation) with the corresponding RUs is clearly seen.
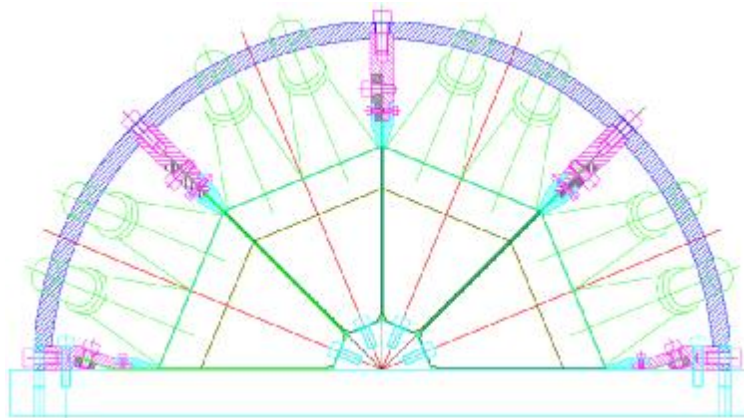
Figure 2.3. Front view of half of the CASTOR calorimeter design (CASTOR EDR, 2007)

The calorimeter will be positioned at 14.385 m from the interaction point. As we mentioned above, covering the pseudo rapidity range of $5.1 \leq \eta \leq 6.6$, the η-range covered will be $5.3 \leq |\eta| \leq 6.46$ for the electromagnetic section with 99% containment and $5.25 \leq |\eta| \leq 6.31$ for the hadronic section with 95% containment. The later η range provides complete overlap with the HF calorimeter (see CASTOR EDR, 2007). The Figure 2.4 shows the pseudo rapidity coverage of full CMS calorimeters. It can be seen that, CASTOR is a unique calorimeter which can serve as both electromagnetic and hadronic calorimeter in the corresponding pseudo rapidity range.
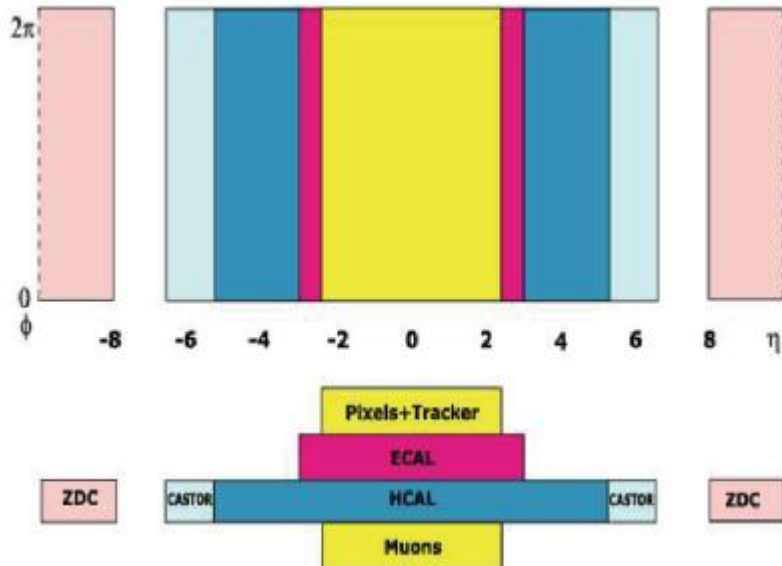
Figure 2.4. Pseudo rapidity coverage of the CMS detector.

The calorimeter is constructed in two semi-circular sections of 4-octants each, in order to be positioned around the fixed beam pipe. Figure 2.5 shows the positioning of the calorimeter in the CMS forward region. Now, the calorimeter is being constructed and assembled at CERN in order to be installed to CMS before the first p-p run.
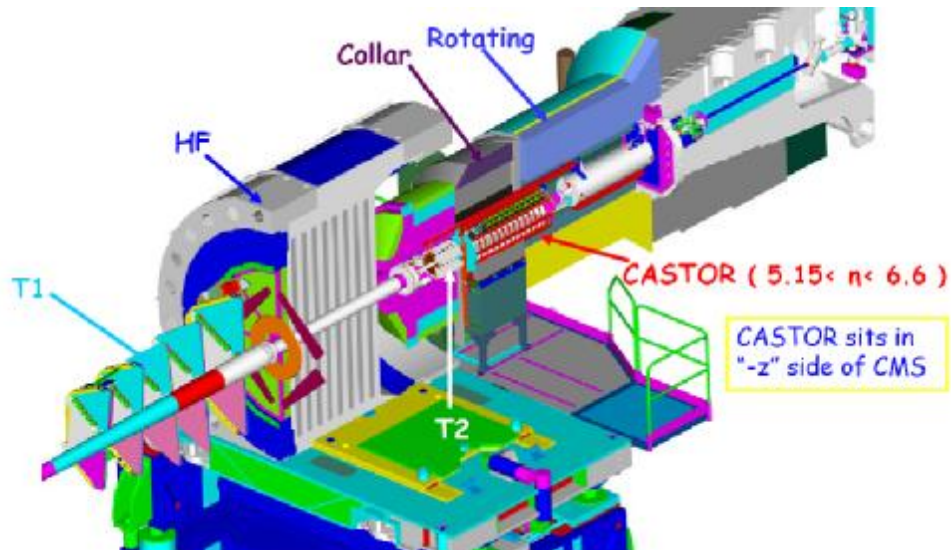
Figure 2.5. Position of CASTOR Calorimeter in CMS (Panagiotou, 2007)

2.2. Physics with CASTOR Calorimeter

2.2.1. Introduction

In general, the addition of CASTOR to the CMS experiment results in a substantial enhancement of its physics potential, as several important observations in p-p, p-Pb and Pb-Pb interactions would either be impossible or seriously diminished without CASTOR. Originally designed as a calorimeter dedicated to the search of exotic events in heavy ion collisions, CASTOR has a rather broad physics program, associated with the very forward rapidity region. It will contribute mainly to the QCD studies, such as diffractive, low-x physics and multi-parton interactions, offering the ability to test the non perturbative region of QCD at Bjorken-x of the order of $10^{-6}-10^{-7}$, as well as to Quark-Gluon Plasma and cosmic-ray physics topics. Of special interest are also specific discovery physics topics associated with Higgs, BSM studies and strangelets.

2.2.2. QCD Oriented Physics

2.2.2.1. Multiple Parton Interactions and Underlying Event

In pp collisions, multiple interactions can occur between the partons of the colliding beam protons, hence we can distinguish between a "hard scattering" component, i.e. the two outgoing hard jets and the so called "underlying event" which consists of the beam-beam remnants plus initial and final-state radiation. Multiple parton scattering contributes to the "underlying event", adding an uncertainty in the interpretation of certain hadronic final states which could be produced either by new physics (Higgs or SUSY) or via multiple parton interactions. Energy-flow measurements as well as trigger on the deposited energy in CASTOR will serve as a tool for the better understanding of the dynamics of multiple interactions and the structure of the underlying event, further helping to tune existing

MC QCD generators. Figure 2.6. is a schematic view of the way that QCD Monte-Carlo models simulate a proton-antiproton collision in which a hard 2-to-2 parton scattering with a certain transverse momentum occurs.
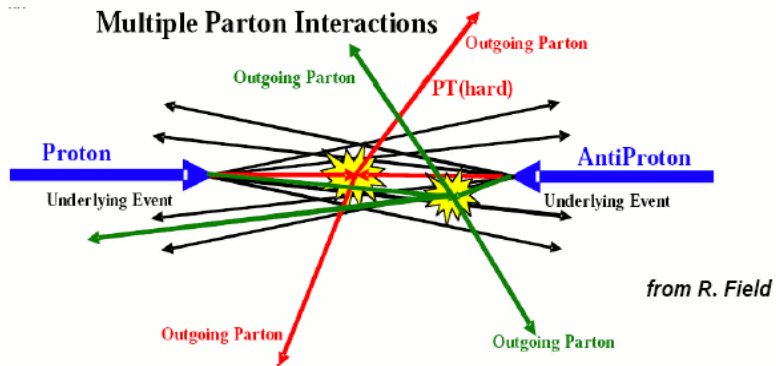
Figure 2.6. Schematic view of PYTHIA's model of the "underlying event" in a proton-antiproton collision with multiple parton interactions (Affolder, 2002).

2.2.2.2. Low-*x* Physics; Parton Saturation

The LHC will operate at such high energies and luminosities that unprecedented low-*x* values will be reached, with the possible production of hard probes such as jets, heavy quarks or Drell-Yan pairs. The measurement of forward jets (pp→j X) or Drell-Yan pairs (pp→l$^+$l$^-$ X) within CASTOR's eta coverage offers the possibility to study the proton Parton Distribution Functions (PDFs) at very small parton momentum fractions (x~10^{-6}). In contrast to the fast rise of the PDFs seen in e-p collisions at HERA, at such low-*x* values, the number of gluons is so large that non-linear (gg fusion) QCD effects become important, however not described by the linear DGLAP or BFKL equations, leading to parton saturation (Heavy Ion Physics TDR, 2007).
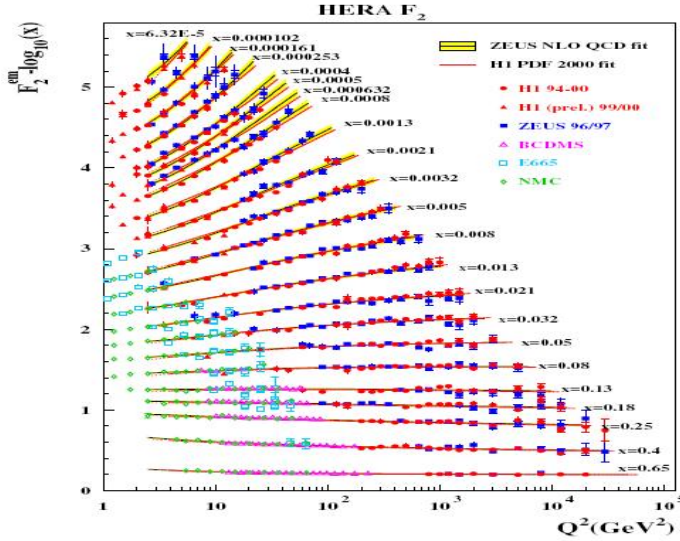
Figure 2.7. $F_2(x,Q^2)$ structure function measured at HERA in proton DIS and fixed target experiments. A strong rise of F_2 as well as scaling violation is evident at small x (D'Enterria, 2007).

The existence of two CASTOR detectors on either side of the interaction point also offers the ability to measure jets with a large separation ("Mueller-Navelet" dijets), which serve as an optimal probe of BFKL and gluon saturation evolution at low-x (Mueller and Navelet, 1987).

2.2.2.3. Diffractive QCD

CASTOR can contribute significantly to the study of diffractive processes. Due to the exchange of two-gluons in a colour singlet state, diffractive events are characterised by one or both protons remaining intact after the interaction (pp→pp X). Those protons are separated by a large rapidity gap from the reaction products (Arneodo and Diehl, 2005) and CASTOR can serve as a precious experimental tool in tagging such rapidity gaps, due to the extended rapidity coverage that the calorimeter offers. Because of the relatively high rate of diffractive events – their cross section accounts approximately to 1/4 of the total p-p cross section – a reliable measurement of soft & hard diffractive interactions is important for a correct projection of the expected pile-up activity in high-luminosity p-p scenarios.
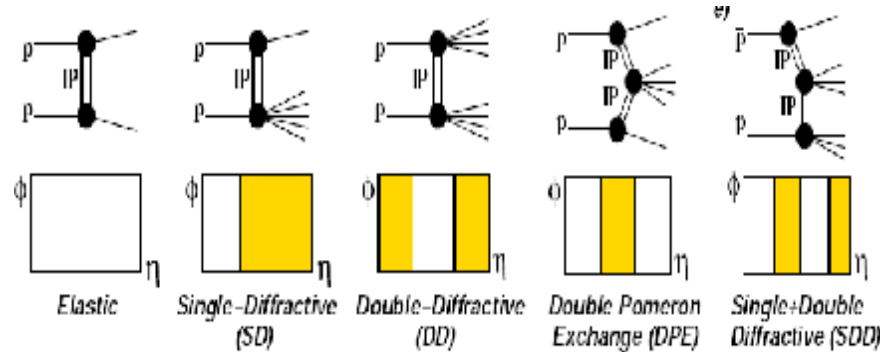
Figure 2.8. Rapidity gaps for difractive scattering (D'Enterria, 2007).

2.2.2.4. Heavy Ion Physics

The CASTOR forward coverage and fast response allows to optimally use this device in the basic L1 trigger and centrality determination for heavy-ion collisions at the LHC (CASTOR EDR, 2007). As can be seen from Figure 2.9, the pseudorapidity region of CASTOR is of great importance for the study of heavy-ion collisions, since although a relatively small number of particles will be produced within its acceptance, they will carry a large fraction of the total energy flow.
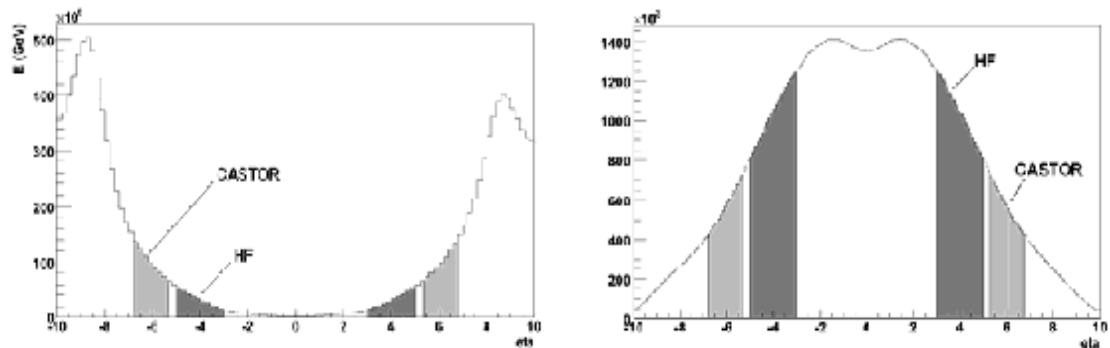
Figure 2.9.The distribution of number of particles (right) and energy (left) distribution as a function of the pseudorapidity in Pb-Pb collisions.

The impact parameter of the colliding ions shows a monotonic correlation with the transverse or total energy, hence CASTOR can provide an estimate of the

event centrality through the measurement of the energy deposited within its forward eta window $5.1 < \eta < 6.6$. The resolution of the impact parameter is measured around 0.6 fm, using only the total energy deposited in the forward region of CASTOR (D' Enterria et al., 2007).
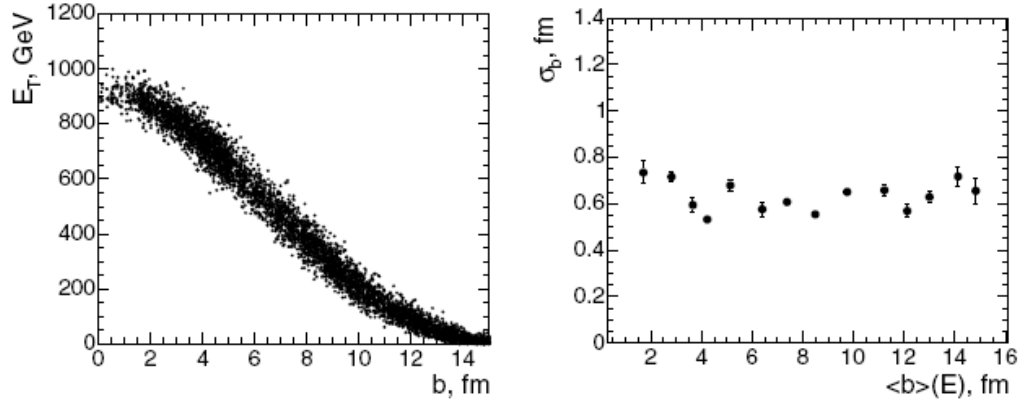
Figure 2.10.Left: Tranverse energy deposited in CASTOR as a function of the impact parameter. Right: Impact parameter resolution using the total energy deposited in CASTOR (Heavy Ion Physics TDR, 2007).

The Pb-Pb particle multiplicities, measured through their energy in the CASTOR rapidities, are in the "limiting fragmentation" range where the Colour-Glass-Condensate (CGC) approaches predict a reduced hadron density. Also, this kinematic regime is characterised by a relatively large net baryonic content, so that CASTOR can provide a unique view of the baryochemical-potential dependence of the properties of the QGP produced in Pb-Pb collisions. Another topic where CASTOR will play an important role is the study of hard probes at forward rapidities, extending the studies that will be made for the pp runs.

2.2.3. Discovery Physics

2.2.3.1. Higgs Physics

The dominant process for Higgs production is gluon-gluon fusion, nevertheless, the vector boson fusion (VBF) process where quarks radiate virtual W bosons to form a Higgs (pp → qqH), has also a large cross section at all plausible Higgs masses. The VBF process is favored for a Higgs of mass greater than around 130 GeV because the two quarks which radiate the W pair which then fuse to make the Higgs continue in the forward/backward direction and can be detected as "tag jets". The final state contains two jets at small angles with respect to the proton beams and a Higgs at wide angles. CASTOR can contribute to the study of the VBF production mode by offering the ability of jet reconstruction/tagging in an extended pseudorapidity range, especially when combined with the HF calorimeter. Based on the dN/dn distribution of VBF quarks, the jet tagging efficiency with CASTOR included can be increased by 15% (see Figure 2.12.) (D'Enterria, 2007).
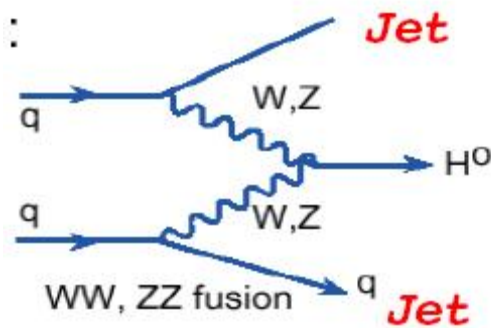
Figure 2.11. Feynman diagram of the VBF production mode (D'Enterria, 2007)
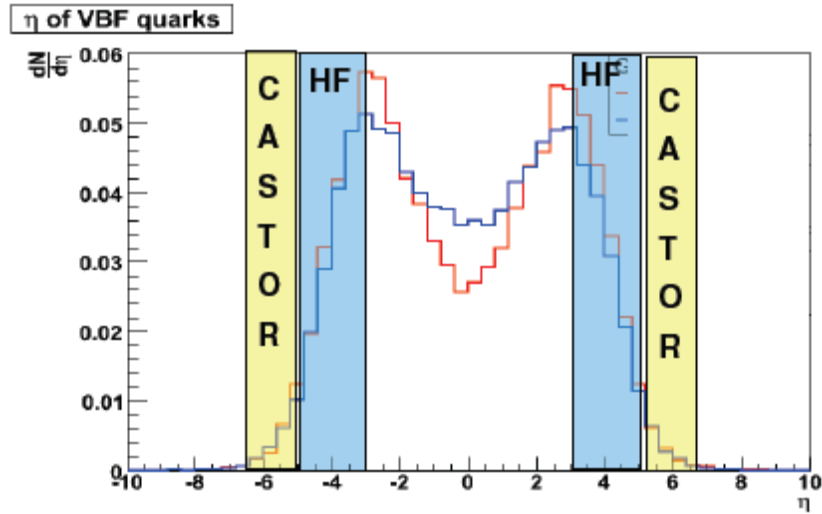
Figure 2.12. CASTOR contribution to a 15% increase of jet tagging efficiency when combined with the HF calorimeter (D'Enterria, 2007).

2.2.3.2. BSM Physics

Many "new physics" signals are characterized by a large amount of missing transverse energy (MET). In order to search for such BSM signals, the hermiticity of the detector is one of the most critical parameters. CASTOR will extend the coverage of CMS from $\Delta\eta$~10 to $\Delta\eta$~11.5 (or 13 with two calorimeters) allowing one to measure more precisely the amount of MET in proton-proton collisions, even though CASTOR is not segmented in pseudorapidity.

2.2.3.3. Centauro's and Strangelets

The first track of Centauro related events have been discovered in high-altitude emulsion chamber experiments. The Pamir experiment, at an altitude of 4400 meters, was the first to observe this type of events. The Chacaltaya experiment of Brazil-Japan collaboration, conducted in the Bolivian Andes at altitude of 5200 meters, described and confirmed in detail a "Centauro" event. These reported events

contain few particles but which are almost all hadronic, accompanied by very few photons. They show that at these high energies (~700 TeV), hadrons can be generated without neutral pions or eta mesons which decay into photons (The mysteries of cosmic rays, http://cerncourier.com/cws/article/cern/).

The name of Centauro came from Greek mythology. A Centaur was asymmetric, with the half of the body a man and the other half a horse by analogy with Centauro event which is almost free of photons and has long penetrating hadronic components. A Centauro-type event is basically characterized by high imbalance between the hadronic and photonic component, which is difficult to explain. Many models have been proposed for their explanation, although the exotic nature of those events still remains.
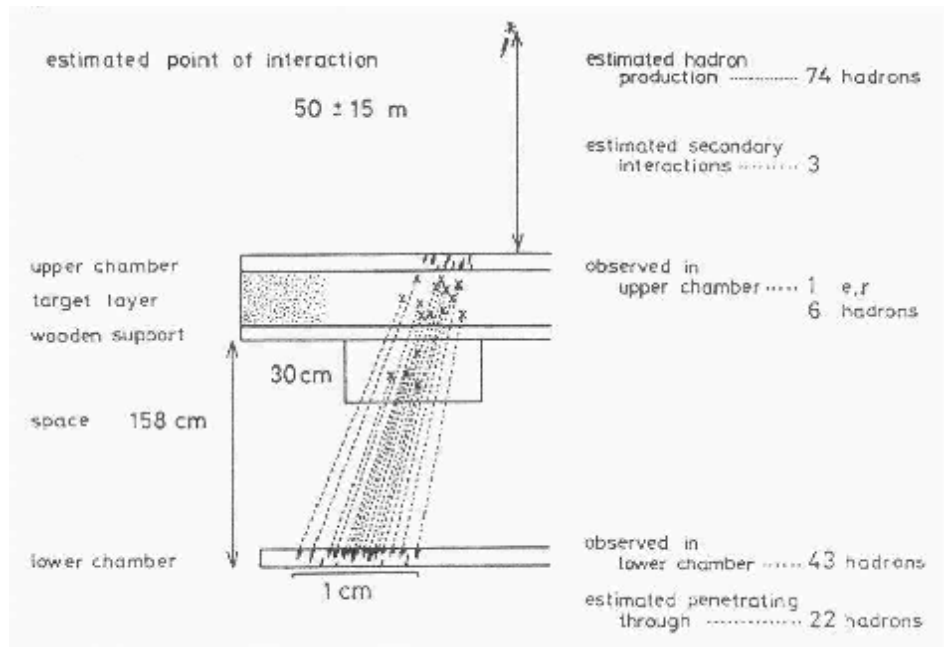
Figure 2.13. Illustration of Centauro I in Chacaltaya experiment (Gladysz-Dziadus, 2001).

The results obtained from Pamir and Chacaltaya experiments showed that hadronic components indicate the existence of several types of Centauro species. These types are characterized by the following features (Gladysz-Dziadus, 2001):

1) abnormal hadron dominance in multiplicity and energy content,

2) low total hadron multiplicity in comparison with an expected event having the same energy in nucleus-nucleus collisions,

3) higher transverse momentum of produced particles and high energy range, for threshold energy of their production ~1000 TeV,

The Centauro events can be divided into several groups with respect to their characteristics, such as:

- Centauros of original type called Centauro I,

- Mini-Centauros,

- Chirons,

- Geminions.

It is obviously difficult to explain these abnormal events. One possible mechanism for the production of Centauro events is the formation of a quark-gluon plasma, incorporated in scenarios with strange quark matter in heavy ion collisions.
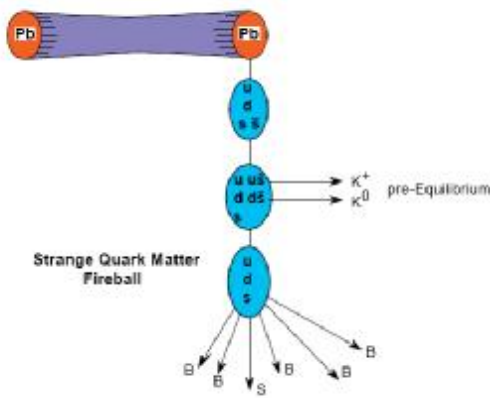
Figure 2.14. Schematic drawing of time evolution of Centauro fireball (Gladysz-
             Dziadus, 2001).

The development and evolution of the Centauro fireball can be seen in Figure
2.14 schematically. A phenomenological SQM model is proposed, explaining the
basic characteristics of Centauro events. The essential points of this model are
discussed below, in association with the long–flying component of Centauro-type
events (Gladysz-Dziadus, 2001).

1. **Formation of a quark–matter fireball.**

The fireball is created in central collisions of ultrarelativistic cosmic–ray
nuclei with air nuclei, in the baryon–rich fragmentation region. When created, it
consists of u, d quarks and gluons only. The fireball has initially very high matter
density and high energy. Large baryochemical potential suppresses the production of
$\bar{u}$ and $\bar{d}$ quarks because the very high baryochemical potential does not allow the
creation of $u\bar{u}$ and $d\bar{d}$ quarks. The dominant mechanism is the gluon-fusion $g \rightarrow s\bar{s}$

.**2. Chemical equilibrium**

During the relaxation time for gluon fusion state, the fireball has a chance to
emit many $K^+(\bar{s}u)$ and $K^0(\bar{s}d)$ mesons carrying away all strange antiquarks and
positive charge. Emitted kaons decrease also the initial temperature and entropy.

Kaons are quickly emitted due to their small mass and high thermal velocity. They are not observed in the ground detectors because they are lost in electro-nuclear cascade process due to their decay producting to mesons in the atmosphere.

3. Strange quark matter state

After emitting kaons the Centauro fireball is a mixture of u, d and s quarks. Without u and d anti-quarks, s quarks cannot be emitted quickly. This may cause a light strange quark-matter state. The fireball is still characterized by very large density, low temperature and low value of charge to mass ratio compared to the original quark–matter fireball. The fireball has a finite excess of s–quarks and as a result of this, it may become a long–lived strangelet, capable to travel a long distance before decaying.

4. Hadronization

The Centauro fireball finally can decay into non–strange baryons and strangelet(s) having very high strangeness. The strangelet temperature is expected to be lower than that estimated for Centauro fireball. Strangelets can be identified as highly deep-penetrating particles in detector materials, frequently accompanying the exotic cosmic–ray events. This scenario is based on the experimental Centauro characteristics derived from five "classical Chacaltaya Centauros" (Gladysz-Dziadus, 2001).

One of the primary goals of CASTOR detector is the search for droplets of strange quark matter (SQM), so called "*strangelets*", which are expected to be produced in Pb-Pb collisions. The existence of stable SQM was first proposed by Witten (Witten,1984), who also suggested the possibility of strangelets being produced by neutron stars, which could convert to more stable SQM stars and possibly reach the Earth.

Generally, SQM could have important cosmological consequences, as it is for example proposed to explain the dark matter problem. It has also been suggested that strangelets are associated with the long penetrating component observed in the Centauro cosmic ray events (Asprouli et al., 1994; Gladysz-Dziadus, 1997).

Many models have been proposed in order to describe strangelet production in heavy ion collisions, essentially via two main mechanisms: production by coalescense of hyperons or following a quark-gluon plasma (QGP) formation. In the latter case, strangelets are regarded as the cooled remnants of a QGP.

Heavy-ion experiments allow to test the production of strangelets, which could be formed in the hot and dense environment of two colliding nuclei. Strangelets are expected to be produced in the very forward region and within CASTOR's eta coverage. This is assumed to be a preferred region to create a dense quark matter fireball, because it is baryon-rich.

Figure 2.15. shows the probability of Centauro and strangelet detection versus the pseudorapidity, as well as the energy of the produced strangelets (Gladysz-Dziadus, 2005), as derived from a Monte Carlo generator for Centauros based on a phenomenological model (Angelis et al., 2004).
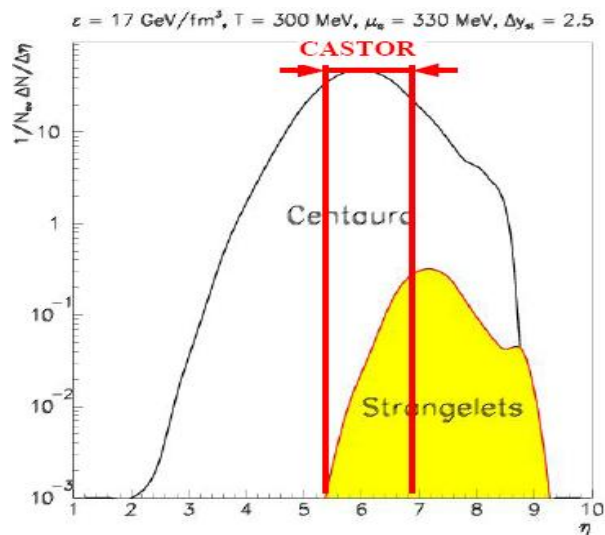
Figure 2.15. Left: Probability of Centauro and strangelet detection versus the pseudorapidity. A large fraction of the Centauro fireball decay products and strangelets are within CASTOR's acceptance (Gladysz-Dziadus, 2001).

The signal produced by strangelets is expected to be clearly different from that produced by normal electromagnetic or hadronic particles populating conventional events. The main signature of strangelets is the relatively low attenuation of their signal, which could be high even at the very end of the calorimeter, exhibiting an extended longitudinal profile. The energy of a strangelet should also be concentrated within a narrow sector of the calorimeter. Figure 2.16 shows the characteristic abnormal transition curves of stable strangelets, compared to the background estimated by means of the HIJING generator (Panagiotou et al, 2007).
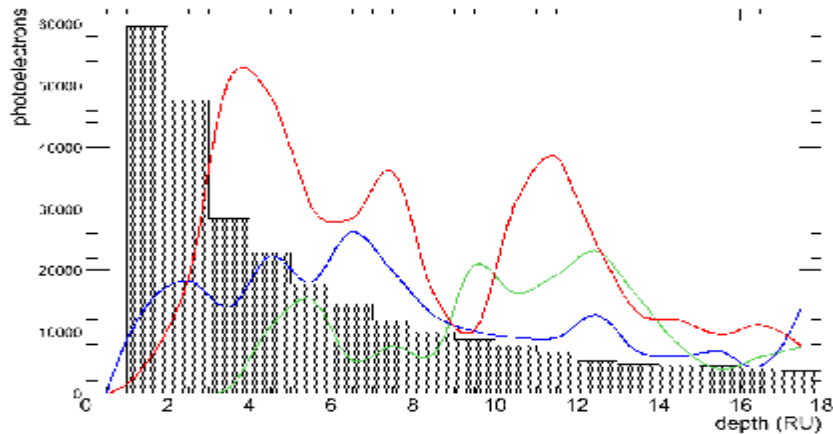
Figure 2.16.Longitudinal profile of the signal produced by strangelets of various energies, E=6 TeV (green), E=8 TeV (blue) and E=12 TeV (red), compared to the background estimated with the HIJING generator (Panagiotou and Katsas, 2007).

3. MATERIAL AND METHOD

3.1 Calorimeters

Calorimeters are unique experimental devices in particle physics, whose main role is to measure the energy of particles. Originally invented for the study of cosmic-ray phenomena, the method of calorimetry was initially developed and later perfected for accelerator-based particle physics experiments. A calorimeter is usually designed and constructed in the form of blocks of instrumented material. Incoming particles are fully absorbed within the apparatus and their energy is transformed into a measurable quantity, via interactions of the particles with the detector's material, through electromagnetic or strong processes. The incident particles' interactions produce showers of secondary particles with progressively degraded energy. Their deposited energy, in the active medium of the calorimeter, can then be detected in the form of charge or light, providing a measurement of the proportional energy of the incident particle (Fabjan, 2003).

Calorimeters are especially useful in present-day experiments because of their following main advantages (Virdee, 1998):

1. They can measure the energies of both neutral and charged particles.
2. They are essentially the only devices that can measure the energies of jets.
3. In a calorimeter, the shower development is different, longitudinally and laterally, for electrons/photons, hadrons and muons, hence they can also be used for particle identification.
4. Calorimeters are experimental devices with potentially fast response.
5. The longitudinal depth which is required to fully contain the showers only increases logarithmically. In comparison, the size for magnetic spectrometers scales as $\sqrt{p}$ for a constant dp/p.
6. Assuming that an experiment has full geometric coverage, calorimeters can also provide indirect detection of neutrinos, using the information from the missing transverse energy.

7. Because of the statistical nature of the cascade development, the energy resolution of calorimeters improves with increasing energy of the incident particle, as $1/\sqrt{E}$. Therefore calorimeters are very well suited to high-energy physics experiments. In contrast, the momentum resolution of magnetic spectrometers deteriorates linearly with the particle momentum (Fabjan, 2003).

Calorimeters can be divided into two different types: electromagnetic and hadronic. Electromagnetic calorimeters are used to measure mainly the energy of electrons and photons through their electromagnetic interactions, while hadronic calorimeters, on the other hand, are used to measure the energy of hadrons by means of their strong and electromagnetic interactions with the material used for detection. According to their construction methods, they can be classified as homogeneous and sampling calorimeters.

3.1.1. Homogeneous Calorimeters

Homogeneous calorimeters, consist of only one type of material that is at the same time used for the energy degradation and the signal production. They are broadly used because they are characterized by much better energy resolution, compared to the one achieved with sampling calorimeters. On the other hand, hadronic calorimeters are not so effective when position measurements and particle identification are needed. They are rarely used as hadronic calorimeters in accelerator experiments due to the fact that they contain the whole shower, consisting of several interaction lengths. Therefore, they are more suitable for neutrino and astroparticle physics experiments in which large volume of material (water or air) is needed to construct the calorimeter in order to detect rare events. Homogeneous calorimeters can be divided into four classes: semiconductor calorimeters, Cherenkov calorimeters, scintillator calorimeters and noble liquid calorimeters.

3.1.2. Sampling Calorimeters

Sampling calorimeters are made of successive layers of an absorber, i.e. a dense material which is used to produce the showers and degrade the energy of the incident particle, and an active medium that provides the detectable signal. The energy resolution of sampling calorimeters is in general worse than the one obtained with homogeneous calorimeters. This is due to the fact that they are characterized by sampling fluctuations, produced by absorber layers interchanged with the active material. On the other hand, sampling calorimeters are relatively easy to segment longitudinally and laterally, therefore they usually provide better spatial resolution and particle identification than the homogeneous detectors. They are in use at accelerators to measure hadronic showers, because they can have enough interaction lengths with a reasonable detector thickness.

Sampling calorimeters can be classified, according to the type of active medium, into scintillation, gas, solid-state, and liquid calorimeters. In the first case the signal is collected in the form of light, whereas in all other cases, it is in the form of electric charge. Commonly used absorber materials are lead, iron, copper and uranium (Fabjan, 2003).

3.2. Shower Development in the Calorimeters

3.2.1. Electromagnetic Shower Development

Electromagnetic particles lose their energy through following mechanisms:

-bremsstrahlung,

-pair production,

-ionization,

-Compton scattering.

Relativistic charged particles lose their energy in the matter by means of Coulomb interaction with atomic electrons. The Bethe-Bloch formula describes the energy loss per unit of length, for charged particles:

$$-\frac{dE}{dx}\bigg|_{ion} = N_A \, \frac{Z}{A} \, \frac{4\pi\alpha^2(\hbar c)^2}{m_e c^2} \, \frac{Z_i^2}{\beta^2} \left[\ln\frac{2m_e c^2\gamma^2\beta^2}{I} - \beta^2 - \frac{\delta}{2} \right]$$

(3.1)

The average energy lost by electrons in lead is shown in Fig.3.1 as a function of energy. It can be seen that, for energies above 10 MeV, the main source of electron energy loss is bremsstrahlung. In this energy range, photon interactions produce mainly electron-positron pairs. For energies above 1 GeV both of these processes become roughly energy independent. At low energies, electrons lose their energy mainly via collisions with the atoms and molecules of the material thus giving rise to ionization and thermal excitation. The main process for the energy loss of photons is Compton scattering and the photoelectric efect (Fabjan, 2003).
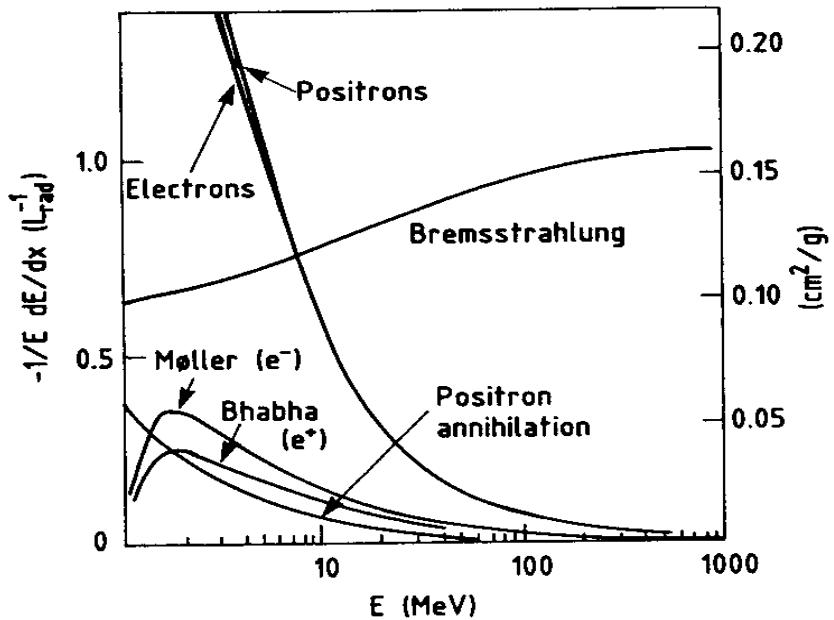
Figure 3.1. Energy loss of electrons and positrons in lead as a function of their energy (Fabjan, 1987).
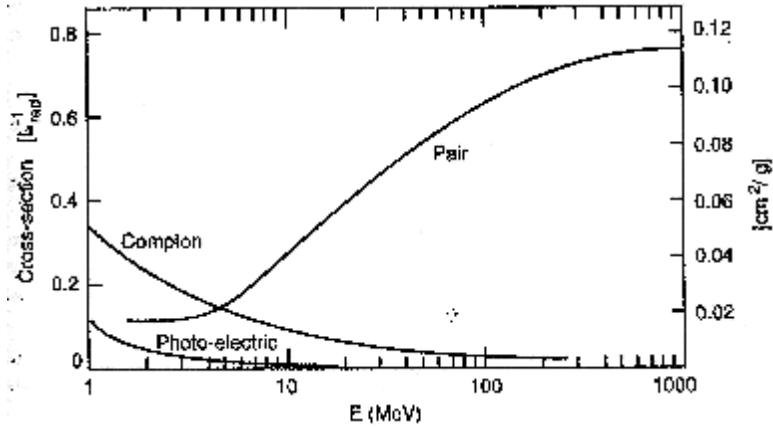
Figure 3.2. Photon interaction cross-section in lead as a function of energy
(Fabjan, 1987).

As a consequence, electrons and photons of sufficiently high energy (≥ 1 GeV) impinging on a block of material, produce secondary photons by bremsstrahlung, or secondary electrons and positrons by pair production. These secondary particles in turn produce other particles by the same mechanisms, thus giving rise to a cascade (shower) of particles with progressively lower energies. The number of particles in the shower increases until the energy of the electron component falls below a critical energy ϵ, where energy is mainly dissipated by ionization and excitation and not in the generation of other particles. The schematic electromagnetic shower development can be seen in Figure 3.3.
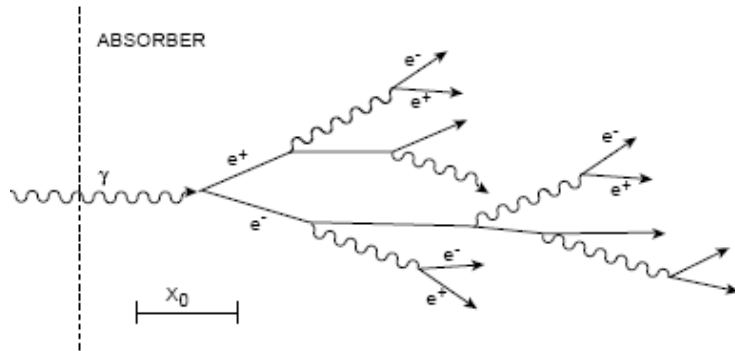
Figure 3.3. Schematic of electromagnetic shower development in matter
(Virdee, 1998).

One of the main features of the calorimeters can be described in terms of the *radiation length* (X_0) parameter, which defines the longitudinal and lateral size of the shower. The radiation length depends on the characteristics of the material and is approximately given by (Particle Data Group, 2002):

$$X_0(\text{g/cm}^2) = \frac{716\,\text{g cm}^{-2}\,A}{Z(Z+1)\ln(287/\sqrt{Z})} \tag{3.2}$$

where Z is the atomic number and A is the atomic mass in g/mole. It defines the mean distance over which a high-energy electron loses all but $1/e$ of its energy by bremsstrahlung, and is equal to the 7/9 of the mean free path for pair production by a high-energy photon. The critical energy also depends on the material and it is given by,

$$e = \frac{610(710)\,\text{MeV}}{Z+1.24(0.92)} \tag{3.3}$$

for solids (gases). Figure 3.1 shows that the critical energy is ~7 MeV in lead.

The transverse size of an electromagnetic shower is mainly due to multiple scattering of electrons and positrons away from the shower axis. Bremsstrahlung photons emitted by these electrons and positrons can also contribute to the shower spread. A measurement of the transverse size, integrated over the full shower depth, is given by the Moliere radius (R_M), (Fabjan, 2003) which can be approximated by,

$$R_M(\text{g/cm}^2) \cong 21\text{MeV}\frac{X_0}{e\,(\text{MeV})} \tag{3.4}$$

Approximately, 90% of the shower energy is contained in a radius of one R_M.

3.2.2. Hadronic Shower Development

The incidence of a high energy hadron in a calorimeter produces a shower of particles due to inelastic collisions with nucleons of the absorber's nuclei. Secondary particles are produced, mainly pions and nucleons, in multiplicity which increases logarithmically with energy per collision. On the average 1/3 of the produced pions are π^0's, that subsequently decay into photons and generate electromagnetic showers. The fraction of the energy of hadrons that does not dissipate in particle production is lost through interactions of excitation of nuclei. Generally this type of interaction does not contribute to signal production (Mavromanolakis, 2003).
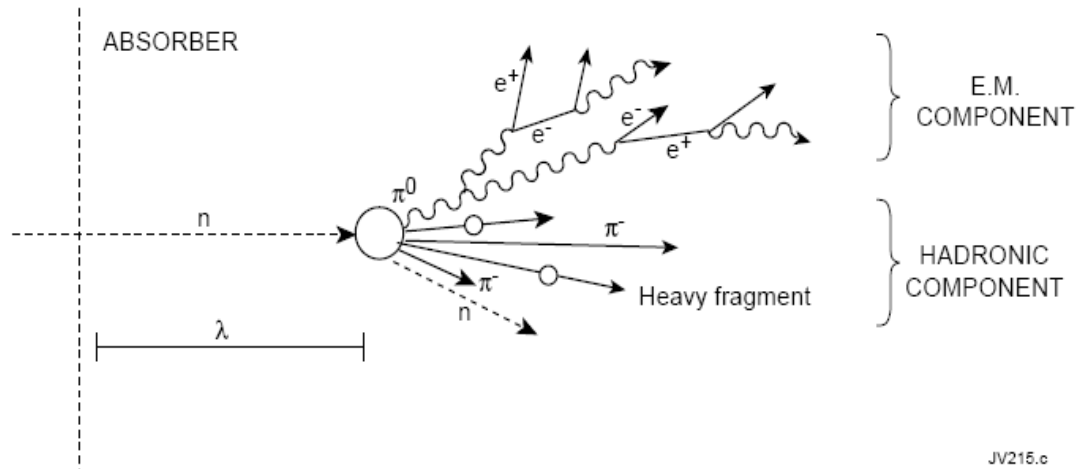
Figure 3.4. Schematic of development of hadronic showers (Virdee,1998)

The characteristic length which governs the longitudinal development of the hadronic showers is the interaction length, λ_I. In a way similar to the radiation length for electromagnetic showers, it is defined as the mean distance that a hadron traverses to lose $(1 - 1/e)$ of its energy in inelastic collisions.

The transverse shower development does not scale with interaction length but one interaction length contains almost 95% of the shower energy in a cylinder of radius R_M.

Mentioned parameters for different materials are listed in Table 3.1.

Table 3.1. Physical properties of some materials used in calorimeters (Virdee, 1998)

	Z	ρ g.cm^{-3}	I/Z eV	$(1/\rho)\mathrm{d}T/\mathrm{d}x$ MeV/g.cm^{-3}	ε MeV	X_0 cm	λ_{int} cm
C	6	2.2	12.3	1.85	103	≈19	38.1
Al	13	2.7	12.3	1.63	47	8.9	39.4
Fe	26	7.87	10.7	1.49	24	1.76	16.8
Cu	29	8.96		1.40	≈20	1.43	15.1
W	74	19.3		1.14	≈8.1	0.35	9.6
Pb	82	11.35	10.0	1.14	6.9	0.56	17.1
U	92	18.7	9.56	1.10	6.2	0.32	10.5

3.3. Characteristics of the Calorimeters

3.3.1. Energy Response and Linearity of EM Calorimeter

The calorimeters are built up to detect the particles and to measure their energy deposition which is proportional to the energy loss in the active volume by incident particles. If the calorimeter is large enough to absorb the radiation completely, then this information can be used to calculate the amount of energy deposition. Depending on the design of the calorimeters, this information may or may not be preserved as the signal is generated.

In most cases, the output electrical signal of the detectors is in the form of current pulse. The amount of ionization is then reflected in the electrical charge

contained in this signal i.e., the integral of the pulse with respect to time. This integral is directly proportional to the amplitude or "pulse height" of the signal, so that this characteristic may be used instead. The relation between the energy deposition and the total charge or pulse height of the output signal is referred to as the "response" of the calorimeter (Leo, 1994).

In an ideal calorimeter, the expectation is that this relation should be linear. For many calorimeters, the response is linear or almost linear for one type of particle but not for another particle. Hence, a calorimeter can have a different response to different types of particles.

3.3.2. Energy Resolution of an EM Calorimeter

In principle, the measured energy with an electromagnetic calorimeter is proportional to the energy of incident particles deposited in the calorimeter. The total track length of the shower T_0, defined as the sum of all ionization tracks due to all charged particles in the cascade, is proportional,

$$T_0 \, (\text{g/cm}^2) \propto X_0 \frac{E_0}{e}$$

(3.4)

The above formula shows that a measurement of the signal produced by the charged tracks of the cascade provides a measurement of the original particle energy E_0. This measurement can be performed, for instance, by detecting the light produced in a scintillating material, or by collecting the charge produced in a gas or in a liquid (Fabjan, 2003).

Generally, the intrinsic energy resolution of calorimeters is given by,

$$\frac{s}{E} = \frac{p_0}{\sqrt{E}} \oplus \frac{p_1}{E} \oplus p_2$$

(3.5)

The symbol $\oplus$ indicates a quadratic sum. The first term is the 'stochastic term', and includes the shower intrinsic fluctuations; the second term is the 'noise term'; and the third term is the 'constant term'. The relative importance of the various terms depends on the energy of the incident particle. Therefore the optimal calorimeter technique can be very different for experiments operating in different energy ranges, since the energy resolution is dominated by different contributions. These contributions are discussed below:

Stochastic term (p_0) : This term is due to the fluctuations related to the physical development of the shower namely depends on the signal generating processes. In sampling calorimeters, the energy deposited in the active medium fluctuates because of the active layers are interleaved with absorber layers. These fluctuations are called 'sampling fluctuations' and represent the most important limitation to the energy resolution of electromagnetic calorimeters. Moreover, these fluctuations are due to variations in the number of charged particles which cross the active layers.

Noise Term (p_1) : This contribution to the energy resolution comes from the electronic noise of the readout chain because of noise contribution from capacitance and dark current and depends on the detector techniques and on the features of the readout units. The noise contribution increases with decreasing energy of the incident particles and at energies below a few GeV may become dominant.

Constant Term (p_2) : This term includes contributions which do not depend on the energy of the particle. Instrumental effects that cause variations of the calorimeter response with the particle impact point on the detector give rise to response nonuniformities such as mechanical imperfections. Additionally, contributions of inter-calibration errors and non-uniformity of signal generation or signal collections are also deteriorating factors of the energy resolution.

In addition to these contributions, the lateral, longitudinal leakage, upstream energy losses and non-hermetic coverage of calorimeters are also the factors that should be considered.

3.3.3. Energy Leakage

Energy leakage, from the calorimeter volume used for the energy measurement, leads to a degradation of energy resolution. It is dominant at high energies. Figure 3.5 illustrates this longitudinal and lateral energy leakage for a homogeneous LXe calorimeter (Virdee, 1998). Longitudinal leakage clearly has more serious consequences. The fraction of the incident energy leaking out of the detector, and the fluctuation on it, increases with energy since the depth at which the shower maximum occurs increases with energy, due to the fact that the proportion of energy deposition increases logarithmically with the incident particle energy.
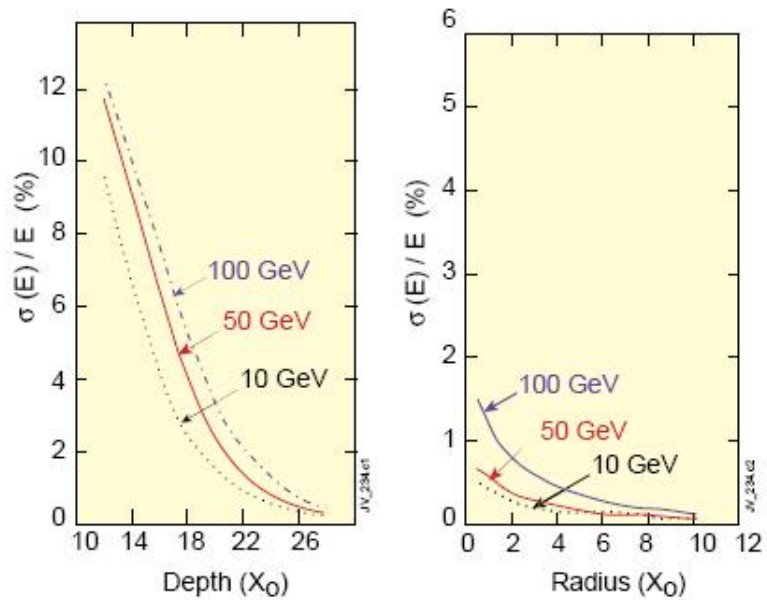
Figure 3.5. The effect of longitudinal and lateral leakage on energy resolution of LXe calorimeter (Virdee, 1998)

The loss of energy resolution due to the lateral energy leakage is smaller since the lateral profile of energy deposition differs much less from one shower to another.

The energy dependence of the fluctuation is also weak as the lateral shower shape is almost independent of energy especially at high energies (Virdee, 1998).

3.4. CASTOR Calorimeter 2003-2004 Beam Tests

3.4.1. Introduction

The first successful performance studies of prototypes for the CASTOR calorimeter were carried out in 2003 and 2004, at CERN/SPS, with electron, muon and pion beams of various energies. The first test beam served as a generic test of different configurations of the calorimeter, including only an EM section with several combinations of structures for the active material of the calorimeter (quartz plates and fibers), various light-guide reflecting materials (glass and foil reflectors) and different light-sensing devices (photo-multipliers and avalanche photodiodes). The prototype II, instrumented for the 2004 test beam, was the first to test the hadronic section of the calorimeter, its design was very close to the final design of the detector. In the following sections, results from both test beams are presented in detail.

3.4.2. Beam Test 2003 of CASTOR Prototype I

A CASTOR prototype was constructed and tested with electron beams at the H4 beamline of SPS in the summer 2003. Figure 3.6 shows a generic view of the prototype. The purpose of the test beam was not to provide precise quantitative results of the response of the calorimeter, but to investigate and compare results from different component options. Two structures of the quartz active material were tested for comparison, one consisting of quartz fibers and one using quartz plates, as well as two different types of reflectors for the light guides, glass and and reflecting foil. For the choice of light sensing devices, two different types of Avalanche Photodiodes (APD) and photomultipliers (PMT) were considered (Aslanoglou et al, 2006). Figure 3.6 shows the configuration options that were investigated. In section 3.4.1 the

various arrangements of the active (quartz) and passive (tungsten) materials of the calorimeter are presented. Section 3.4.2 discusses the light transmission efficiency of different combinations of light-guides and reflectors. Section 3.4.3 summarizes the characteristics of the light-sensing devices tested.
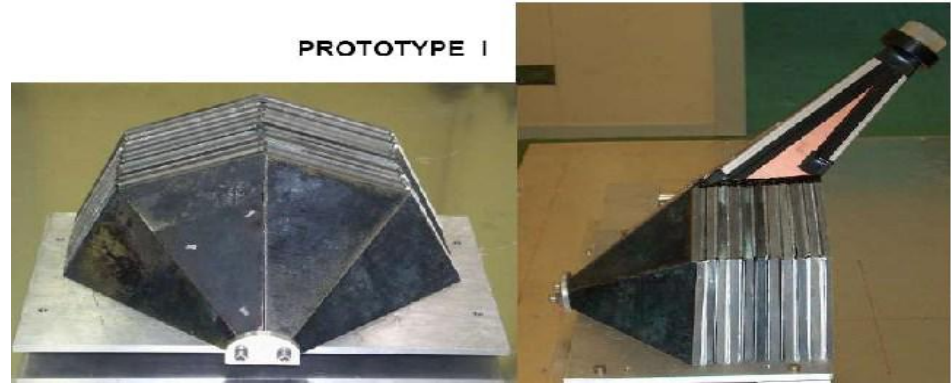
Figure 3.6. Left: frontal view of CASTOR prototype I. Right: lateral view of the prototype I and one of the light guides that were used (Aslanoglou et al., 2006)
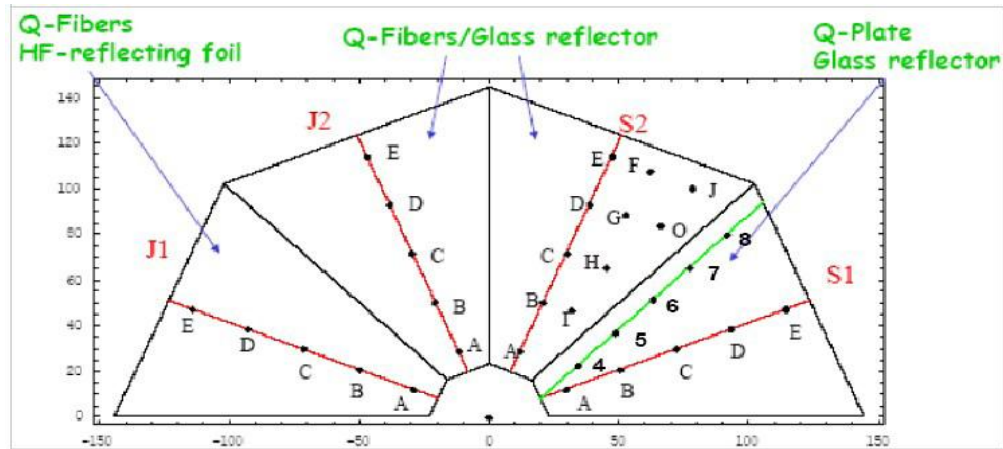
Figure 3.7. Schematic view of different configuration options investigated in the 2003 test beam. The points A-E and 4-8 are scan locations used in calorimeter response uniformity studies (Aslanoglou et al., 2006).

3.4.2.1 Sensitive Material and Absorber

The prototype was azimuthally divided into 4 octants and longitudinally segmented into W/Q layers The tungsten and quartz planes were inclined at 45° with respect to the beam axis, in order to maximize the Cherenkov light output. The density of the tungsten plates was ~19.0 g/cm^3 and the total length of each sector was $0.83\lambda_I$ ($23.7X_0$) (Aslanoglou et al., 2006). The response of the calorimeter and the relative energy resolution were studied for quartz fibers (Q-F) and quartz plates (Q-P). Four octant readout units of the calorimeter were tested, arranged side-by-side in four azimuthal sectors. Each readout unit consisted of 10 sampling units, while each sampling unit for sectors J1, J2, and S2 (see Fig. 3.7) was comprised of a 5 mm thick tungsten plate and three planes of 640 μm thick quartz fibers. The quartz fibers were produced by Ceram Optec and had 600 μm pure fused silica core with a 40 μm polymer. The sampling unit for sector S1 consisted of a 5 mm thick tungsten plate and one 1.8 mm thick quartz plate. Both types of quartz active material, fiber or plate, had about the same effective thickness. The filling ratio was 30% and 37% for the quartz fibers and quartz plates, respectively (Aslanoglou et al., 2006).

3.4.2.2 Air-core Light Guides

For the CASTOR prototype I an air-core light-guide was used, made of Cu-plated 0.8 mm PVC (see Figure 3.8). Two different reflecting materials were considered for the internal walls of the light guide: a reflector of 0.5 mm thick float-glass with evaporations of AlO and MgFr, and a Dupont polyester film reflector coated with AlO and enhancing dielectric layer stack SiO_2 +TiO_2 (HF reflecting foil). The light transmittance in the light-guides was studied for both types of reflecting materials.
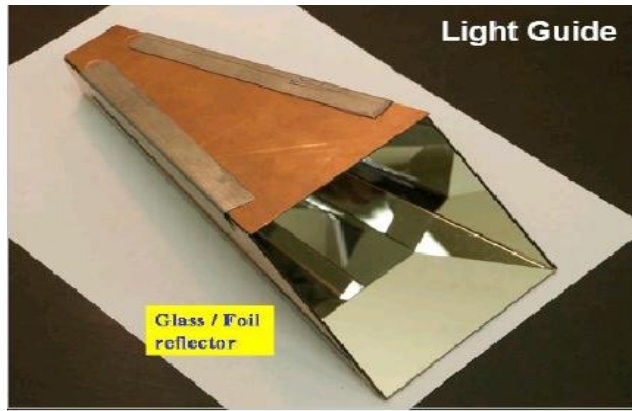
Figure 3.8. Photograph of the light guide used for CASTOR prototype I (Aslanoglou et al., 2006)

3.4.2.3 Readout Devices

CASTOR prototype I incorporated two different types of readout devices: Avalanche Photodiodes (APDs) and photomultipliers (PMTs). Two different kinds of APDs were tested, a Hamamatsu S8148 (APD1) and Advanced Photonics DUV (APD2), as well as two different types of PMTs, the Hamamatsu R374 and Philips XP2978. 4 Hamamatsu APDs, each 5×5 mm^2, were placed in a 2×2 matrix with total area of 1 cm^2. The Advanced Photonics DUV APD had an active area of 2 cm^2. The Hamamatsu and Philips PMTs had both an active area of 3.1 cm^2.

3.4.2.4 Beam Test Results

For the testing of the prototype I, the apparatus was placed on a platform, movable with respect to the electron beam in both horizontal and vertical directions. The beam line was equipped with telescopes of two wire chambers, as well as two crossed finger scintillator counters, positioned in front of the calorimeter, which allowed the determination of the electron impact point.

3.4.2.4.(1). Energy Linearity and Resolution

To study the linearity of the calorimeter response and the relative energy resolution as a function of energy, the central points C (see Figure 3.9) in different azimuthal sectors have been exposed to electron beams of energy 20,40, 80, 100, 150 and 200 GeV. The distributions of signal amplitudes, after introducing the cuts accounting for the profile of the beam, are shown in figures 3.9–3.11, fitted by a Gaussian function.
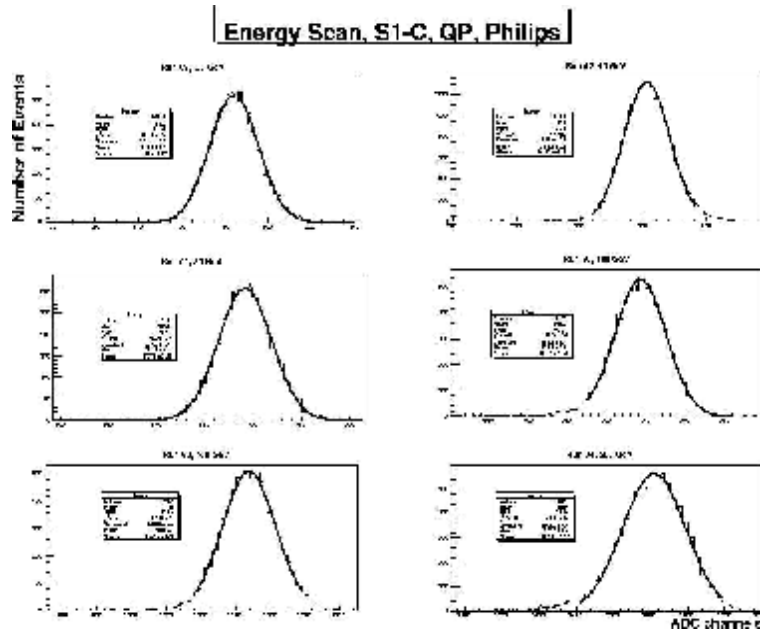
Figure 3.9. Distributions of signal amplitudes in ADC channels for electron beam energies (20, 40, 80, 100, 150 and 200 GeV) impinging on the central point C of sector S1 (Philips PMT) (Aslanoglou et al., 2006).
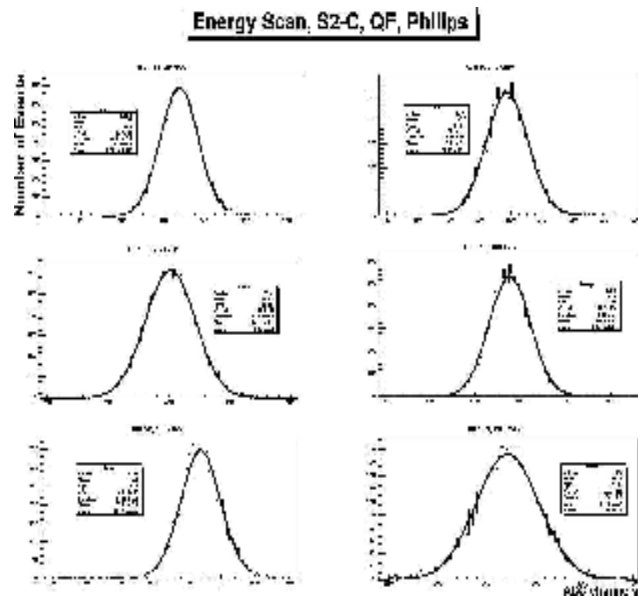
Figure 3.10. Distributions of signal amplitudes in ADC channels for electron beam energies (20, 40, 80, 100, 150 and 200 GeV) impinging on the central point C of sector S2 (Philips PMT) (Aslanoglou et al., 2006).
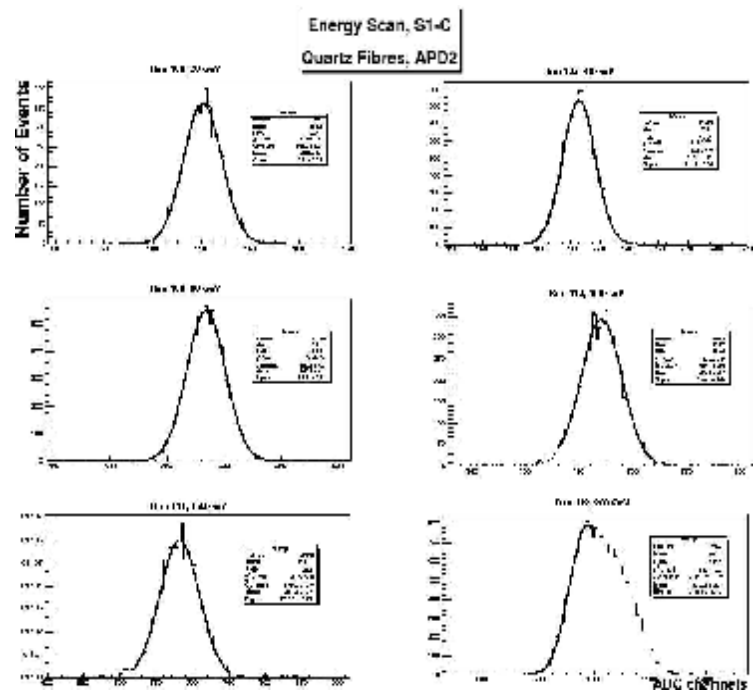
Figure 3.11. Distributions of signal amplitudes in ADC channels for electron beam energies (20, 40, 80, 100, 150 and 200 GeV) impinging on the central point C of sector S1 (Advanced Photonics APD) (Aslanoglou et al., 2006).

Figure 3.12 shows the mean response of the calorimeter as a function of the energy of the incoming electron beam, for all configurations. It can be seen that the response is linear in the energy range explored. The average signal amplitude, expressed in units of ADC channels, can be satisfactorily fitted by the following formula:

$$ADC = a + b \times E \tag{3.6}$$

where the energy E is in GeV. The ADC distributions are not pedestal subtracted (the parameter a gives the pedestal value which is roughly the same for all studied configurations). The fitted values of the parameters for each configuration are shown in Table 3.2.
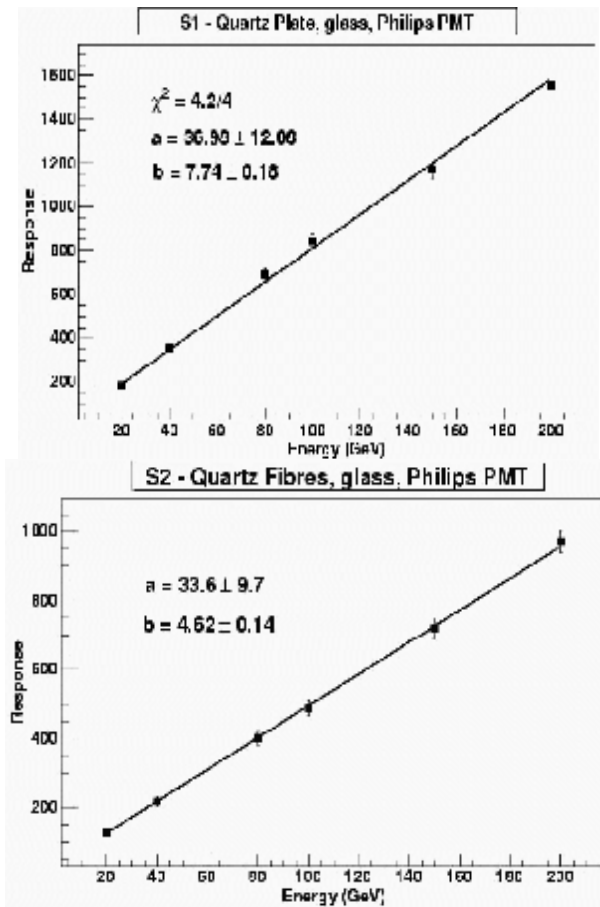
Figure 3.12. Energy linearity in different sectors of CASTOR prototype I: (a) S1 (Philips PMT), (b) S2 (Philips PMT) (Aslanoglou et al., 2006)

The relative energy resolution of the calorimeter was studied by plotting the normalized width of the Gaussian signal amplitudes (see Figures 3.9– 3.11), σ/E, with respect to the incident beam electron energy, E (GeV). The data points were fitted by two different functional forms of (3.5) (Anvizino et al., 1995; Livan et al., 1995).
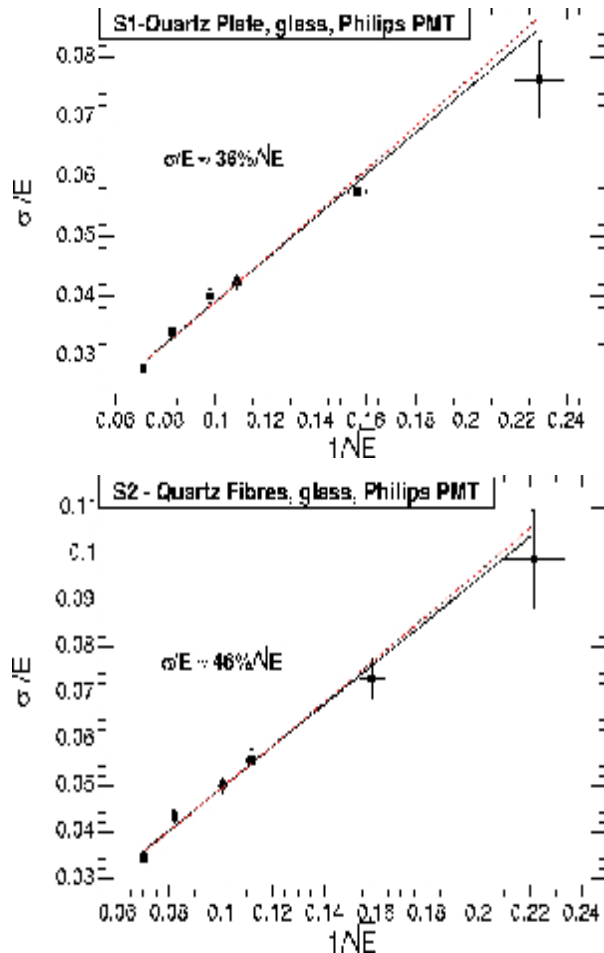
Figure 3.13. Energy resolution of CASTOR prototype I for different configurations in sectors: (a) S1 (Philips PMT), (b) S2 (Philips PMT), The data points were fitted by the functional forms $\sigma/E = p_0 + p_1/E^{1/2}$ (black) and $\sigma/E = p_0 \oplus p_1/E^{1/2} \oplus p_2/E$ (red) (Aslanoglou et al., 2006)

Figure 3.13 shows the plot of the relative resolution as a function of $E^{-1/2}$ and the fit parameters are shown in Table 3.2. It was found that the constant term p_0 was close to zero for all sectors. The measured stochastic term p_1 was in the range 24%-82%. For the avalanche photodiodes the p_2 term is needed, measured to be 1.25 GeV and 4.5 GeV for Advanced Photonics APD and Hamamatsu APD, respectively. The APDs were very sensitive to both voltage and temperature changes, however there was not any monitoring of their stability (Aslanoglou et al., 2006).

Table 3.2. Fit parameters obtained from the functional forms of equation (3.5) for elecktromagnetic resolution of calorimeter prototype I (Aslanoglou et al., 2006)

Sector	*Fit*	Resolution			X^2/ndf
		P_0	P_1 (GeV$^{1/2}$)	P_2 (GeV)	
Q Plates (S1, glass) Philips PMT	(2 p) (3 p)	0.001±0.002 0.010±0.004	0.36±0.02 0.38±0.02	0.01±0.4	6.4/4 7.4/3
Adv.Photonix APD	(2 p) (3 p)	0.017±0.005 0.036±0.006	0.28±0.04 0.24±0.04	1.2±0.2	2.5/3 6.2/2
Q Fibres (S2, glass)	(2 p) (3 p)	0.004±0.003 0.013±0.006	0.45±0.04 0.48±0.02	0.0±0.8	3.2/4 3.7/3
Q Fibres (J2, glass)	(2 p) (3 p)	0.01±0.01 0.04±0.02	1.16±0.13 0.82±0.22	0.45±1.6	4.1/4 1.3/3

3.4.3. Beam Test 2004 of CASTOR Prototype II

The second prototype of CASTOR was constructed and tested in 2004. It consisted of quartz plates, avalanche photodiodes (APDs) as well as photomultiplier tubes (PMTs), and air-core light-guides with inner reflective foil (Dupont polyester film reflector coated with AlO and reflection enhancing dielectric layer stack SiO_2 + TiO_2). A major difference from prototype I was the fact that a new semi-octant (φ =

22.5°) geometry of the readout unit in the electromagnetic section was tested. Figure 3.14 shows a view of prototype II.

One octant sector, consisting of the electromagnetic (EM) and the hadronic (HAD) section was built. Both sections were constructed with successive layers of tungsten plates as absorber and fused silica quartz plates as active medium. The EM part was 14 cm long and divided into two semi-octant sectors, segmented into 2 reading units, i.e 4 independent readout channels in total. The HAD part was 40 cm long with the same octant geometry of prototype I. It was longitudinally segmented into 4 sections. The Cherenkov light produced by the passage of relativistic particles through the quartz medium was collected in reading units along the depth of the calorimeter and focused by air-core light guides onto the photodetector devices, APDs or PMTs (Aslanoglou et al., 2007).
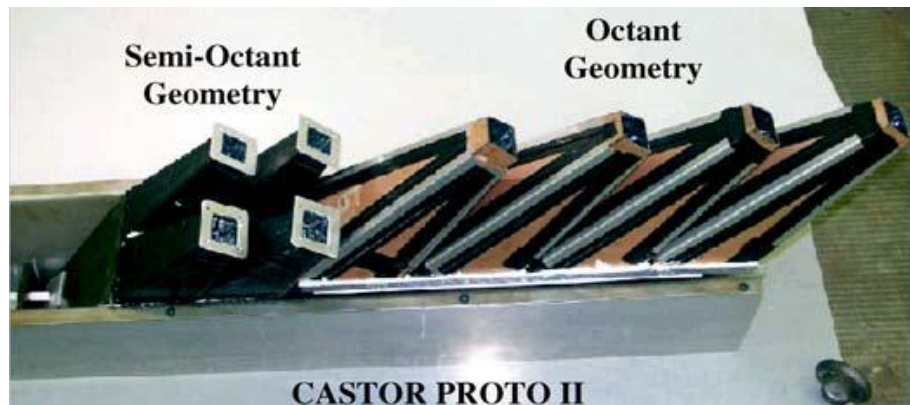
Figure 3.14. View of the CASTOR prototype II before assembling the photodetectors. The EM section was constructed with a semi-octant geometry while the HAD section retained the octant geometry of prototype I (Aslanoglou et al., 2007).

For the electromagnetic section, the W-plates had a thickness of 3 mm and the Q-plates 1.5 mm. For the hadronic section, the W- and Q-plates had a larger thicknesses of 5 mm and 2 mm, respectively. All the plates were inclined 45° with

respect to the direction of the impinging particles, in order to maximize the Cherenkov light output in the quartz. The perimeter sides – except the top one – were painted with white reflecting paint. In the EM section, each readout unit (RU) consisted of 11 W/Q-plates layers corresponding to 13.4 X_0, or 0.536 λ_I. The total length of the EM section corresponded to 26.8 X_0 and 1.072 λ_I lengths. The readout units of the the hadronic section consisted of 10 W/Q-plates layers and were 0.796 λ_I deep, i.e 3.186 λ_I in total. The whole prototype has 4.26 λ_I deep. For some runs with pions, an additional inactive absorber of 1.03 λ_I was placed in front of the calorimeter, in order to make the EM section act as a hadronic one, increasing the total depth of the prototype to 5.3 λ_I (see Aslanoglou et al., 2007).

The Cherenkov light was collected and transmitted to photodetector devices through air-core light-guides. The light guides were equipped with Dupont [AlO+SiO2+TiO2] reflective foil. As photodetectors, a matrix of 4 or 6 Hamamatsu S8148 APDs (developed originally for the CMS electromagnetic calorimeter (Deiters et al., 2001; Antunovic et al., 2005) was used, as well as two different types of PMTs. The total area of the APDs was 1 cm^2 (for 4 APDs) and 1.5 cm^2 (for 6 APDs). The phototubes were positioned only on one side of the EM section of the prototype, for comparison with the APDs. The two types of PMTs used were a Hamamatsu R7899 PMT, and a radiation-hard PMT FEU-187 from RIE St. Petersburg, with cathode area 2 cm^2.

3.4.3.1. Beam Test Results

For the test beam of prototype II, electron, hadron (π^-) and muon (μ^-) beams of several energies were used. The energy response of the electromagnetic and hadronic calorimeter was obtained with energy scans with 20–200 GeV electrons, 20–350 GeV pions, as well as 50, 150 GeV muons. The apparatus was placed on a movable table in both horizontal and vertical (x, y) directions.

3.4.3.1.(1). Electromagnetic Response

The EM section was tested using electron beams of E=20–200 GeV. Figure 3.15 shows a typical ADC spectrum for the 100 GeV electron beam, on the EM section of the prototype, equipped with PMTs. The beam also contained muons, which can also be seen as minimum ionizing particles (MIPs), just above the pedestal. The energy response of the calorimeter was found to be well fitted with a Gaussian for all energies. Figure 3.16 shows the energy response for 20 and 200 GeV electron beams, obtained with 4 and 6 APDs respectively.
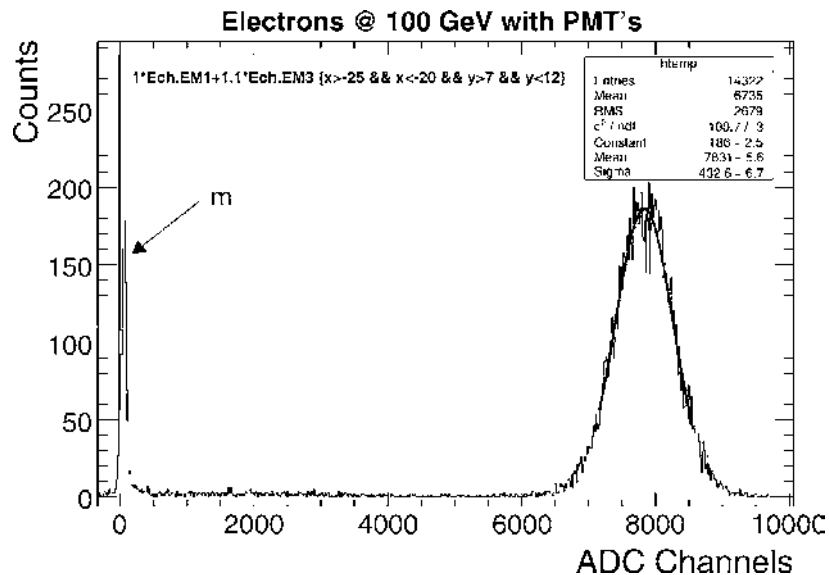
Figure 3.15. Energy response of the EM calorimeter equipped with PMTs to 100
         GeV electrons. The muons signal can also be seen. (see Aslanoglou et al.,
         2007)

In order to check the linearity of the calorimeter, a central point in the two different azimuthal sectors was exposed to beams of various energies. The distributions of signal amplitudes, after introducing the cuts on the spatial profile of the beam (a circle of radius 2 mm), were in most cases symmetric. The peak signal position, obtained for the three photodetector configurations, is plotted as a function

of the beam energy in Figure 3.17. For all configurations, the calorimeter response was found to be linear in the energy range explored.
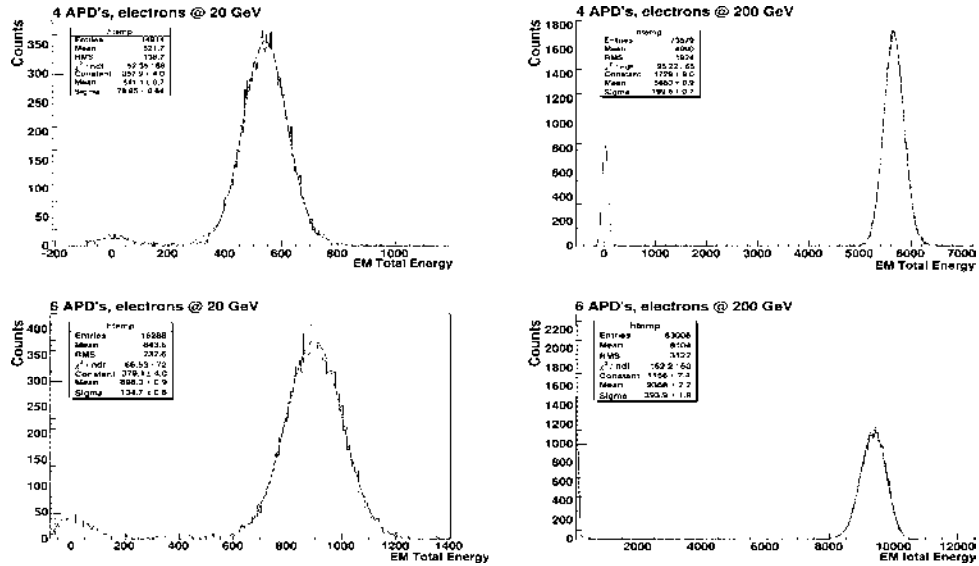
Figure 3.16. Electromagnetic spectra for different beam energies for 4APD's and 6 APD's (Aslanoglou et al., 2007).
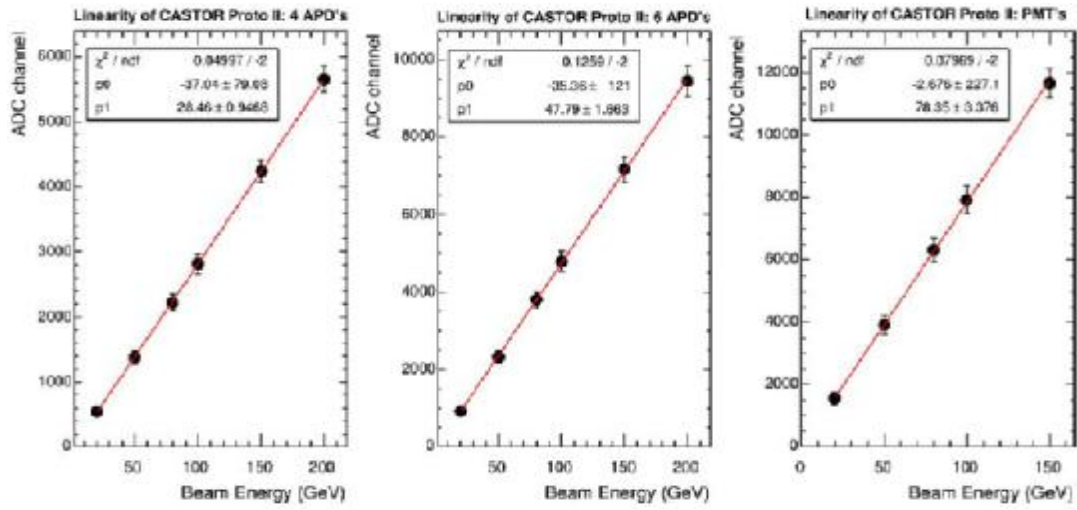
Figure 3.17. Energy response linearity (signal peak-position versus beam energy) of the EM section, obtained with different photodetectors: 4 APDs (left), 6 APDs (center), and PMTs (right) (Aslanoglou et al., 2007).

For all the configurations, i.e. with PMTs or APDs, the response was found to be linear. The constant term was found to be negligible while the signal amplitude was fitted by the formula (3.6).

3.4.3.1.(2). Energy Resolution

The energy resolution was measured by plotting the normalized width of the Gaussian fits of the signal amplitudes, with respect to the incident energy of the electron beam. The data points were found to be satisfactorily fitted by the functional forms (Aslanoglou et al., 2007):

$$\sigma / E = p_0 + p_1 / \sqrt{E} \tag{3.7}$$

$$\sigma / E = p_0 \oplus p_1 / \sqrt{E} \oplus p_2 / E \tag{3.8}$$
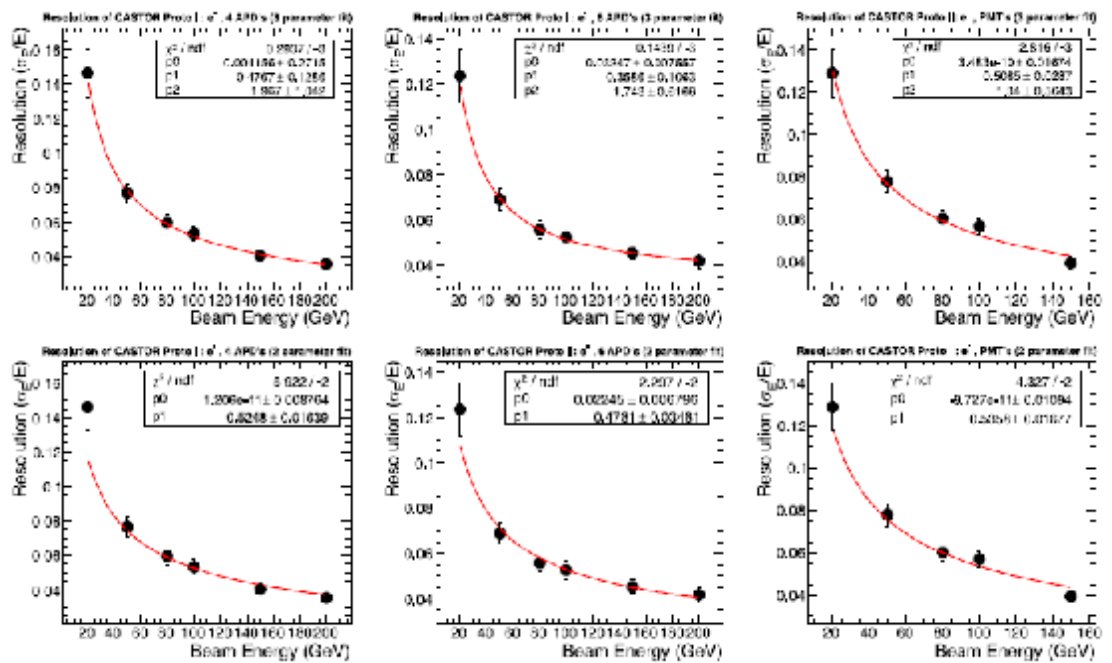
Figure 3.18. Energy resolution of the EM section of prototype III, for three different readout configurations: 4 APDs (left), 6 APDs (center), and PMTs (right). The results are shown for the 3-parameters fit (top) and 2-parameters fit (bottom) (Aslanoglou et al., 2007).

44

Figure 3.18 shows the results for all readout configurations considered. The fit parameters are summarized in Table 3.3. The stochastic term was measured in the range 36-51%, while the constant term was close to zero.

Table 3.3. Energy resolution fit parameters as obtained from the functional forms (3.7) and (3.8) (Aslanoglou et al., 2007).

Photodetector	*Fit*	P_0	$P_1(\text{GeV}^{1/2})$	$P_2(\text{GeV}^{-1})$	χ^2/ndf
4APDs	(3.7)	$1.2\text{x}10^{-11}\pm8.7\text{x}10^{-3}$	0525 ± 0.0163	-	5.92/4
4APDs	(3.8)	$1.1\text{x}10^{-3}\pm0.21$	$0.477\pm9.65\text{x}10^{-2}$	1.97 ± 0.70	0.29/3
6APDs	(3.7)	$2.24\text{x}10^{-2}\pm6.80\text{x}10^{-3}$	0.478 ± 0.0348	-	2.3074
6APDs	(3.8)	$3.25\text{x}10^{-2}\pm7.56\text{x}10^{-2}$	0.358 ± 0.106	1.74 ± 0.62	0.14/3
PMTs	(3.7)	$9.7\text{x}10^{-11}\pm1.1\text{x}10^{-2}$	0.536 ± 0.0168	-	4.33/3
PMTs	(3.8)	$3.5\text{x}10^{-10}\pm1.7\text{x}10^{-2}$	0.508 ± 0.029	1.34 ± 0.56	2.82/2

4. ANALYSIS AND RESULTS

4.1. Introduction

In this section, we describe the active (quartz) and passive (tungsten) materials of the calorimeter considered and assembled for the prototype III. Section 4.2 discusses the components of the prototype III tested in this new study. Then, section 4.3 describes the test beam and gives the test beam analysis results in detail.

4.2. Technical Description of CASTOR Prototype III

4.2.1. Tungsten Plates

The tungsten plates are fabricated by C. A. Starck GmbH. They are made out of tungsten alloy, containing 97% W, 1.3% Fe and 1.7% Ni. The density is 18.5 ± 0.2 g/cm^3. For the EM (HAD) section the thickness is 5 mm (10 mm), but the effective thickness increases to 7.07 mm (14.14 mm) at 45° inclination. The geometry, dimensions, consistency and density of samples of the W-plates were measured by the CERN Metrology Section. (CASTOR EDR, 2007). One of the tungsten plates used in prototype III is shown in Figure 4.1.

Figure 4.1. Example of a tungsten plate used for the assembly of prototype III.

4.2.2 Quartz Plates

The quartz plates are designed in semi-octant geometry and define the 16-fold azimuthal segmentation of the calorimeter. The semi-octant construction designs of the EM and HAD Q-plates are shown in Figures 4.2, 4.3. The two semi-octants (R, L) are positioned side by side along their vertical side and are optically separated by thin Al foils. The light guides are positioned on top of the semi-octant quartz plates (5Q + 5W) to form the RU.

Figure 4.2. 4 mm quartz plates used for the hadronic section of prototype III.

The 4 mm quartz plates for the hadronic section are made from the quartz panes salvaged from the DELPHI-RICH detector. The 345×375 mm^2 panes are taken apart from the original DELPHI bi-tubes by decaying the epoxy resin of the assembly in an industrial furnace at 250°C for 1 hour. The broken panes were used in processing R&D (Research and Development) and 120 pieces plus spares were

used for the construction of the 2007 beam test prototype octant. All panes have the same accurate thickness of 4 mm ± 0.05 mm (CASTOR EDR, 2007)
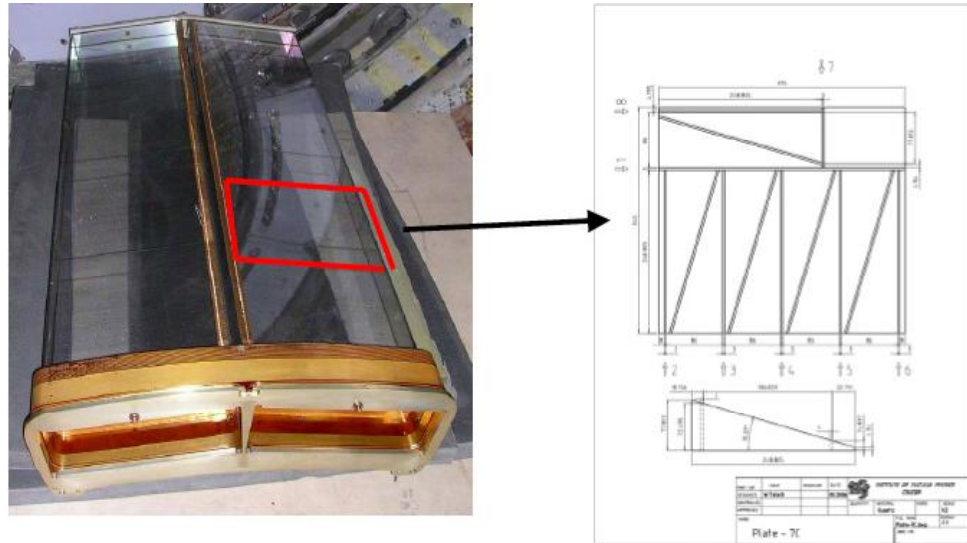
Figure 4.3. Bi-tube breakdown into 16 panes of 10 pieces (CASTOR EDR, 2007).

4.2.3. Processing of the Q-Plates

The production of the HAD quartz plates consists of cutting, lapping and polishing steps. All operations are performed on the machines located in the CMS-ECAL Crystal Laboratory. Specific tooling was designed and manufactured.

4.2.3.1. Cutting of Q-Plates

Panes which have been dismantled from DELPHI-RICH are divided into 10 pieces using a 2 mm thick diamond wheel. The cutting machine used for this operation is shown in Figure 4.4. Cutting is performed in stacks of four pieces for time efficiency. Different tools were used for the processing of the plates (Fig. 4.5, 4.6). The yield of the cutting operations is normally above 95%. The surface finish is better than 2 μm Ra and an extra-thickness of 50 μm is enough for the lapping operation to follow. About 20 cutting operations are necessary to transform a stack

of four panes into 40 pieces. It takes about 20 minutes in average to perform one cutting operation. Tooling changes, stack mounting, adjustments, dismounting, cleaning and machine servicing should be added to this time.

Figure 4.4 Cutting machine and operating panel

Figure 4.5. Cutting of straight edges

Figure. 4.6. Tool for cutting of chamfers

4.2.3.2. Lapping of Q-Plates

Glued stacks of four pieces after cutting are lapped on the edges to reach a surface finish of Ra = 0.2 μm needed for following polishing. Three stacks are held in position in the processing tool (Fig. 4.7). The lapping abrasive is conventional diamond slurry with grain size 15 μm. It takes about 15 min to perform one lapping operation and a thickness of about 50 μm is removed. Three of the four sides are lapped and the small front face is left as cut. There is one tool type for the processing of the two piece sides normal to the large face and one for the inclined side.

Figure 4.7. Lapping machine (upper), Lapping-polishing tool turned upside down to show the edge of 3 stacks after lapping (bottom)

4.2.3.3. Polishing of Q-Plates

The lapping tool with its three lapped stacks is thoroughly cleaned from lapping slime and taken to the polishing operation without additional adjustment. This can be done in parallel to the polishing operation. A suspension of colloidal silica with pH-9 provides the required surface finish (Ra < 0.02 μm) by special chemical affinity to fused quartz. The material removal is of the order of a few μm. It takes about 20 min to perform one polishing operation. Figure 4.8 shows the polishing machine in the laboratory.

Figure 4.8. Lapping machine

4.2.4. Air-core Light Guides

The Cherenkov photons produced in the quartz plates are collected and transmitted to the PMTs by means of air-core light guides. The efficiency of light transmission and its dependence on the light-source position are crucial parameters, which characterize the light guide and significantly affect the performance of the calorimeter. The design and dimensions of the air-core light guides for the

electromagnetic and hadronic sections are obtained from Monte Carlo simulations. For the design of the optimum size of air-core light guides, a GEANT based code was developed to simulate the transmission of Cherenkov photons through a light guide (Aslanoglou et al., 2006). Figures 4.9. (a,b) show the construction drawings of the EM and HAD light guides, respectively. Differences between two light guides can be seen on both figures. The light guide on the EM section is shorter than the HAD one in length.
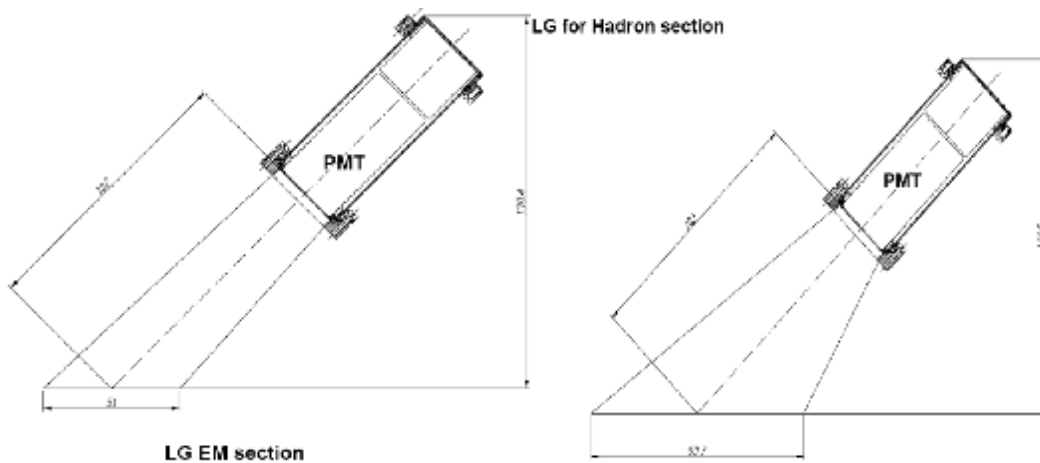
Figure. 4.9. (a). Cross section of the EM light-guide with the PMT and base housing. (b). Cross section of the HAD light-guide with the PMT and base housing (CASTOR EDR, 2007).

Figure 4.10. Air-core light guide designed for prototype III and reflecting foil covering inside

The inside walls of the light guides are covered with reflecting foil for the transmission of the Cherenkov light. The reflecting medium is an aluminum reflector coated with dielectrics SiO_2 and TiO_2. The same is used for the forward hadronic calorimeter of CMS (HF). Tyvek paper is used as a diffuser. In addition, it protects the surface of polished quartz plates from contact with the tungsten ones.

Figure 4.11. Assembly of light guides onto W/Q sampling units of prototype III

4.2.5. Readout Units (Photomultipliers) and Bases

The air core light guides transmit the Cherenkov light to the light-reading devices. For the light collection two different types of PMTs were used: (i) a Hamamatsu R5380Q, and (ii) a radiation-hard multi-mesh FEU-187 from RIE St.

Petersburg, with cathode area ~ 2 cm^2 The RIE phototubes were positioned only on the EM section of the Jura side of the prototype (RUs 2 and 4), for comparison.

Figure 4.12. CASTOR PMTs on top of the light guides and bases used in the 2007 beam tests

Figure. 4.13. PMT base and its cable (CASTOR EDR, 2007)

4.3. Beam Tests 2007 of CASTOR Prototype III

The beam test of prototype III was performed in the H2 line at CERN Super Proton Synchrotron (SPS) during two weeks in Aug-Sept 2007. The energy linearity, resolution and uniformity, as well as the spatial resolution were studied with electrons, pions and muons of various energies. The signal from muons, behaving as MIPs, was exploited for the inter-calibration of all the channels of the prototype. Other special studies included runs with the beam hitting directly on the light-guides and PMTs and observing the readout response, as well as testing the light-output with an optimized cut on the exit surface of the quartz plates.

The prototype III consisted of a full-length octant, containing the electromagnetic (EM) and hadronic (HAD) sections, with a total of 28 readout-units (RUs) (Figures. 4.14, 4.15) constructed with successive layers of tungsten (W) plates, as absorber, and fused silica quartz (Q) plates as active medium.
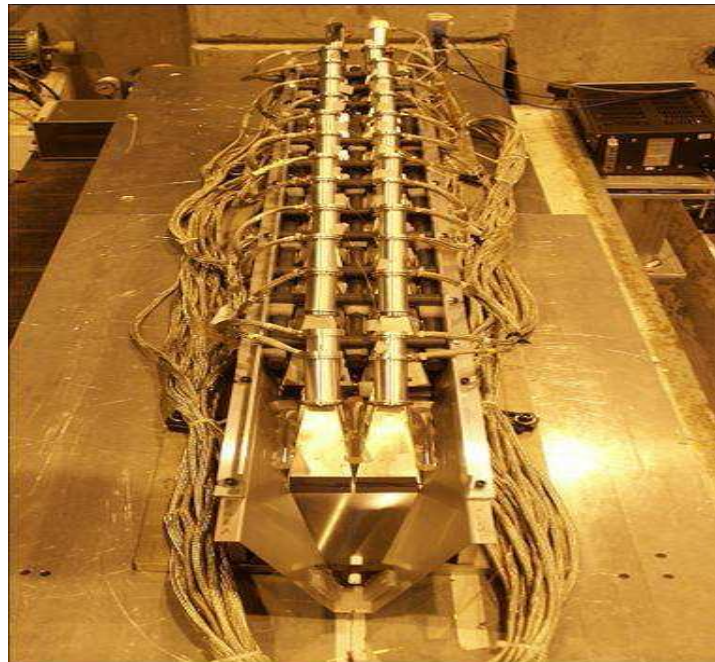
Figure 4.14. The fully instrumented CASTOR octant prototype III. The calorimeter was placed on top of a moving table at the CERN/SPS H2 line.
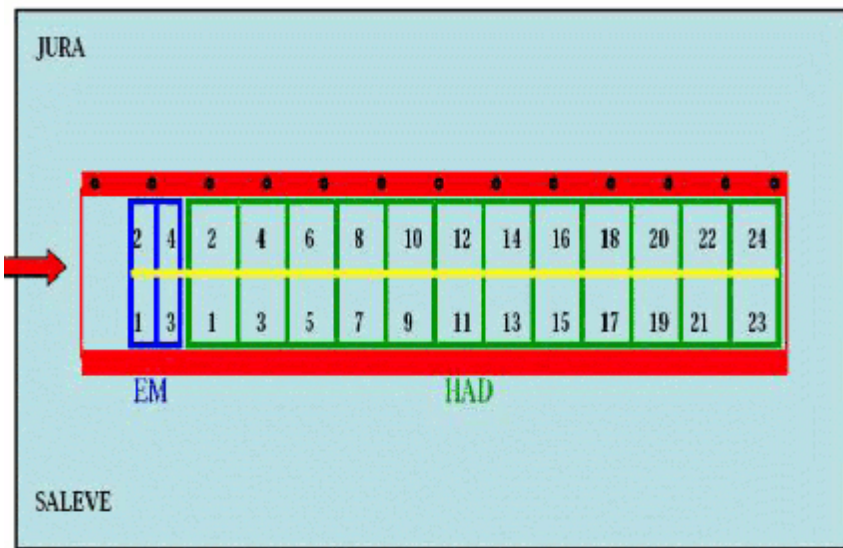
Figure 4.15. Schematic drawing of the 28 readout units (RU's) of CASTOR
prototype III (Aslanoglou et al., 2008).
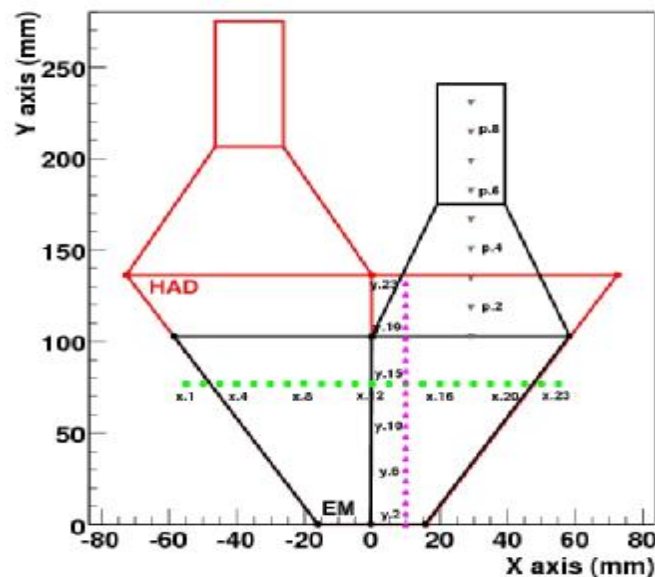
Fgure 4.16. Schematic drawing of the front face of the EM (black lines) and HAD
(red lines) sections onto a 45° vertical plane (Aslanoglou et al., 2008).

Table 4.1. (*x,y*) coordinates of the beam impact points for the horizontal and vertical scans for electron and hadron beams. (Aslanoglou et al., 2008)

Horizontal Scan (Saleve)			Vertical Scan (Saleve)		
Scan points	x(mm)	y(mm)	Scan points	x(mm)	y(mm)
x.13	5	76.88	y.13	10	72
x.14	10	76.88	y.14	10	78
x.15	15	76.88	y.15	10	84
x.16	20	76.88	y.16	10	90
x.17	25	76.88	y.17	10	96
x.18	30	76.88	y.18	10	102
x.19	35	76.88	y.19	10	108
x.20	40	76.88	y.20	10	114
x.21	45	76.88	y.21	10	120
x.22	50	76.88	y.22	10	126
x.23	55	76.88	y.23	10	132

Figure 4.16 shows the two semi-octants of the electromagnetic and of the hadronic sections, projected onto a plane at 45° with respect to the beam axis. We notice that there is no complete overlap of the two sections, due to the different sizes of the W/Q-plates. The horizontal and vertical numbers correspond to distances along the plate (*x-y* coordinates) of the points used for the horizontal and vertical scans. Table 4.1 gives the (*x,y*) coordinates of the impact points that were selected for the horizontal and vertical scans of the prototype, for both electron and pion beams. The location of these points on the 45° projection of the semi-octant sectors is shown in Figure 4.16. The beam profile for each point was subdivided into a number of smaller parts, each of diameter less than 1 cm, so more impact points could finally be used.

A schematic description of the H2 beam line of the SPS at CERN is shown in Figure 4.17. The energy response of the electromagnetic and hadronic sections was obtained through energy scans with: 10-200 GeV electrons, 20-350 GeV pions, as well as 50, 150 GeV muons. The calorimeter was placed on a platform, with the ability to move in both horizontal and vertical (*x,y*) directions. Wire chambers were

installed upstream of the prototype (see Fig. 4.17), giving precise information on the position of each particle hitting the calorimeter. In this way, the selection of particular regions of the beam profile was possible.
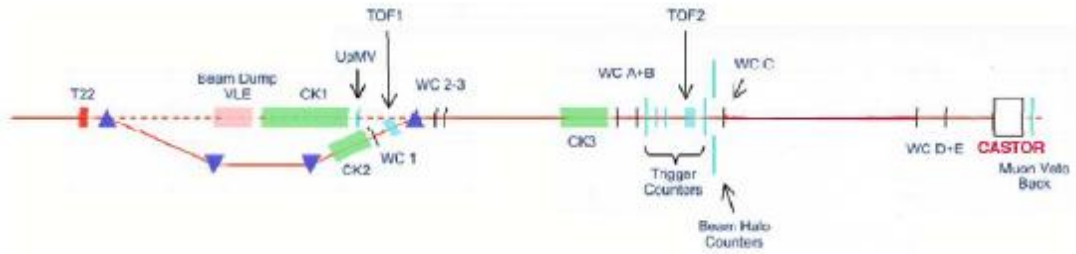
Figure 4.17. Schematic figure of the H2 beam line of the SPS at CERN (Aslanoglou et al., 2008).

4.3.1 Muon Beam and Inter-Calibration of Channels

Muons of $E = 50$ and $E = 150$ GeV were used for the intercalibration of the channels of the prototype III. Figures 4.18, 4.19 show the muon peaks measured for the 150 GeV beam with the Hamamatsu R5380Q and RIE FEU187 PMTs. The muon signal, fitted by a Gaussian distribution, was separated from the pedestal in the EM sections. After the replacement of the quartz plates in the first hadronic section of the Saleve side semi-octant, equipped with the Hamamatsu PMT, the muon signal was also seen clearly in that channel. The good separation between the pedestal and the muon signal peak was exploited in order to intercalibrate the 28 channels of the calorimeter, by using the energy response per channel. Table 4.2 contains the derived intercalibration constants as obtained from the mean signal per channel and from a Gaussian+Landau fit of the muon signal peaks, also shown in Figure 4.20.
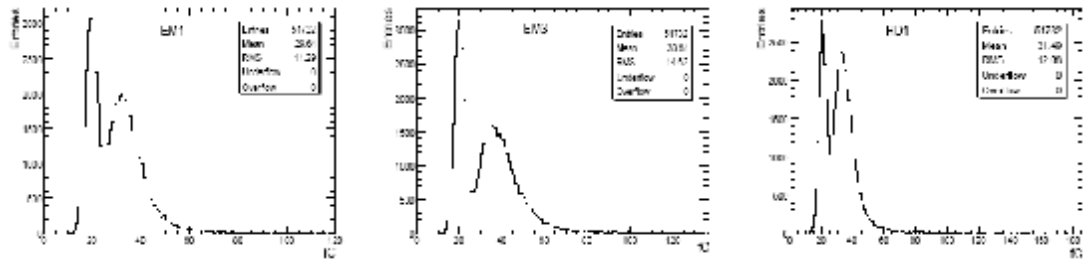
Figure 4.18. The muon spectra measured on EM1, EM3 and HAD1 with Hamamatsu PMTs on Salave side (Aslanoglou et al., 2008)
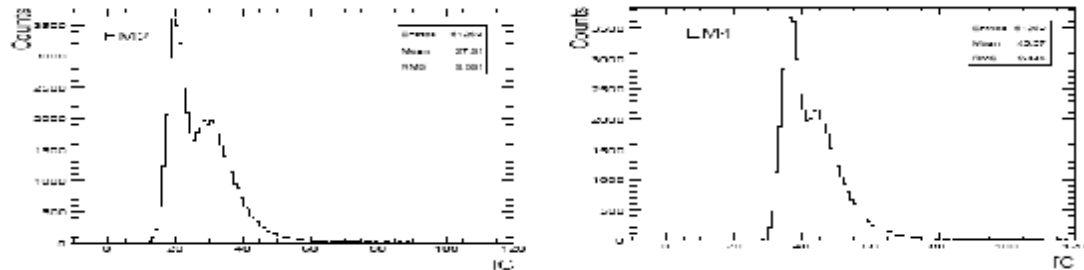
Figure 4.19. The muon spectra measured on EM2 and EM4 with RIE PMTs on Jura side (Aslanoglou et al., 2008)
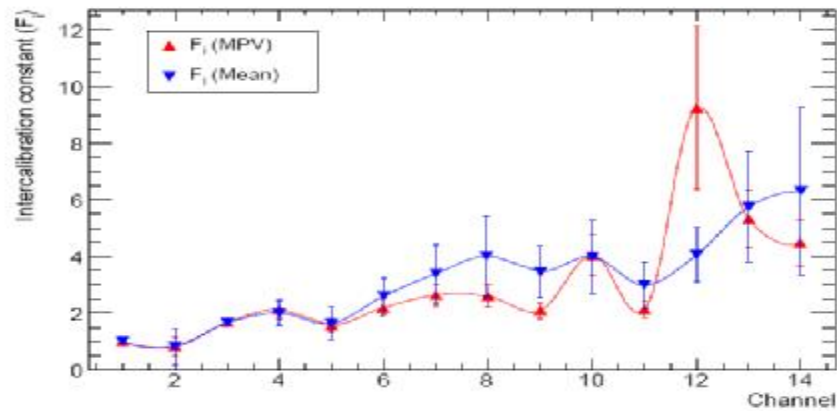
Figure 4.20. Intercalibration constants (F_i) of different channels in the Saleve side semi-octant, derived from the muon energy spectra (Aslanoglou et al., 2008).

Table 4.2. Inter-calibration constants for each channel, calculated using a run with a muon beam of 150 GeV and equation 1. F_i (*MPV*) corresponds to a Gaussian+Landau fit of the spectra, while F_i (*Mean*) corresponds to the mean response for an amplitude range [−50,10000] without any restrictions.(Aslanoglou et al., 2008)

Channel	F_i (MPV)	F_i $(Mean)$
EM1	1.0000 ± 0.0000	1.0000 ± 0.0000
EM3	0.8401 ± 0.0437 (stat)	0.8195 ± 0.0388 (stat) ± 0.0275 (syst)
HD1 (QP at 45°)	2.5137 ± 0.3236 (stat)	2.4876 ± 0.5975 (stat) ± 0.2197 (syst)
HD1 (QP at 90°)	1.6787 ± 0.0843 (stat)	1.6612 ± 0.1531 (stat) ± 0.0132 (syst)
HD3	2.3320 ± 0.3296 (stat)	2.0087 ± 0.400 (stat) ± 0.1862 (syst)
HD5	1.7247 ± 0.2188 (stat)	1.6339 ± 0.4033 (stat) ± 0.4093 (syst)
HD7	2.3881 ± 0.3108 (stat)	2.6066 ± 0.5417 (stat) ± 0.3011 (syst)
HD9	2.8879 ± 0.3649 (stat)	3.3910 ± 0.9397 (stat) ± 0.3564 (syst)
HD11	2.8547 ± 0.3797 (stat)	3.9939 ± 0.8160 (stat) ± 1.1854 (syst)
HD13	2.2996 ± 0.2950 (stat)	3.4543 ± 0.6627 (stat) ± 0.6220 (syst)
HD15	4.4350 ± 0.7447 (stat)	3.9887 ± 0.7839 (stat) ± 0.9968 (syst)
HD17	2.3320 ± 0.3007 (stat)	2.9906 ± 0.5818 (stat) ± 0.5614 (syst)
HD19	10.1370 ± 2.8787 (stat)	4.0573 ± 0.8707 (stat) ± 0.3940 (syst)
HD21	5.8437 ± 1.0153 (stat)	5.7573 ± 1.1246 (stat) ± 1.5886 (syst)
HD23	4.9180 ± 0.8443 (stat)	6.3119 ± 1.2647 (stat) ± 2.6950 (syst)

4.3.2. Electromagnetic Response Linearity

Electron beams of energies 10, 30, 50, 80, 100, 120, 150, 180 and 200 GeV were used to study the energy response linearity and resolution. Figure 4.21 shows typical examples of the electron signal peaks, fitted by Gaussian distributions, as measured in the Saleve side with the Hamamatsu PMTs. For the energy scan of the prototype, a central point on the front face of the calorimeter, for both Saleve and Jura side sectors, was exposed to the electron beam of various energies.
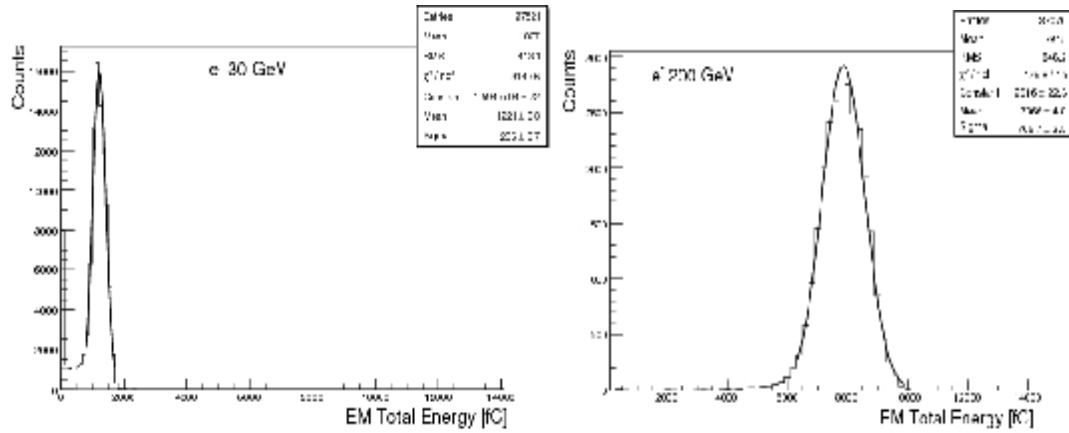
Figure 4.21. Examples of the electron signal peaks for electrons of E=30GeV and
E=200 GeV (Basegmez et al., 2008).

A spatial cut was applied to the beam profile, selecting a circle of radius less than 1 cm. Figure 4.22 shows the beam profile onto the front face of the calorimeter, for an incoming electron beam of $E = 200$ GeV, hitting the right semi-octant (Saleve side), before and after the applied cut. The distribution of the particles in the scintillator-wire-chamber D was used, as it was the closest working wire chamber to the prototype. Figures 4.23 and 4.24 exhibit the signal distribution for the electron beam of $E = 120$ GeV before and after the spatial cut to the beam profile. It can be seen that the available statistics is significantly reduced, while the fit quality is better (see Fig. 4.24).
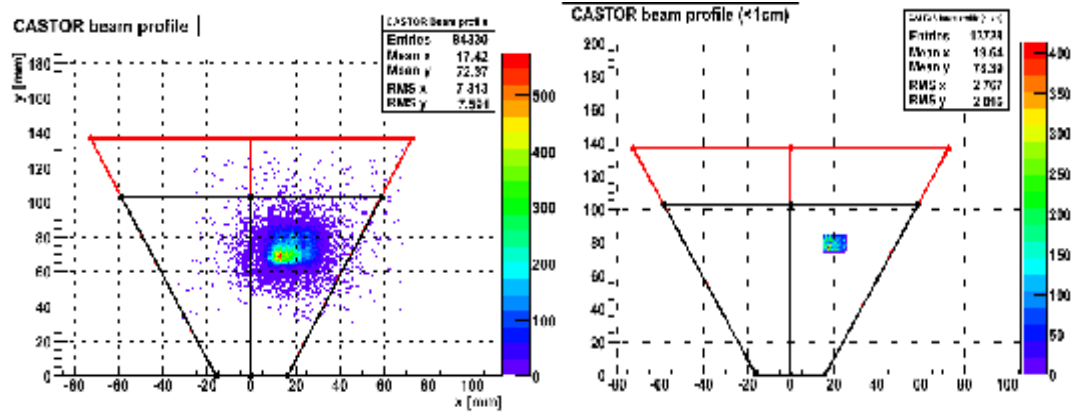
Figure 4.22. Beam profile projected onto the front face of the calorimeter using the hits distribution from the WC-D, before (left) and after (right) a spatial cut (Aslanoglou et al., 2008).
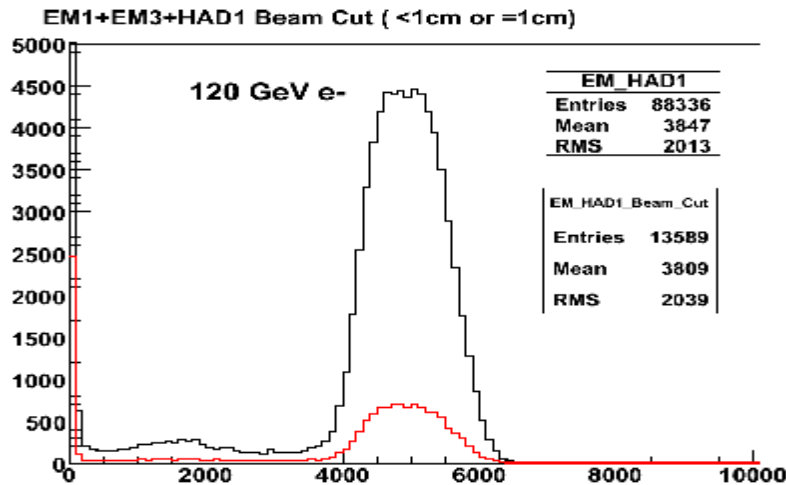

Figure 4.23. Signal distribution of the sum of the signals in EM1, EM3 and HAD1 channels, before (black) and after (red) a 1cm × 1cm spatial cut on the beam profile.

63
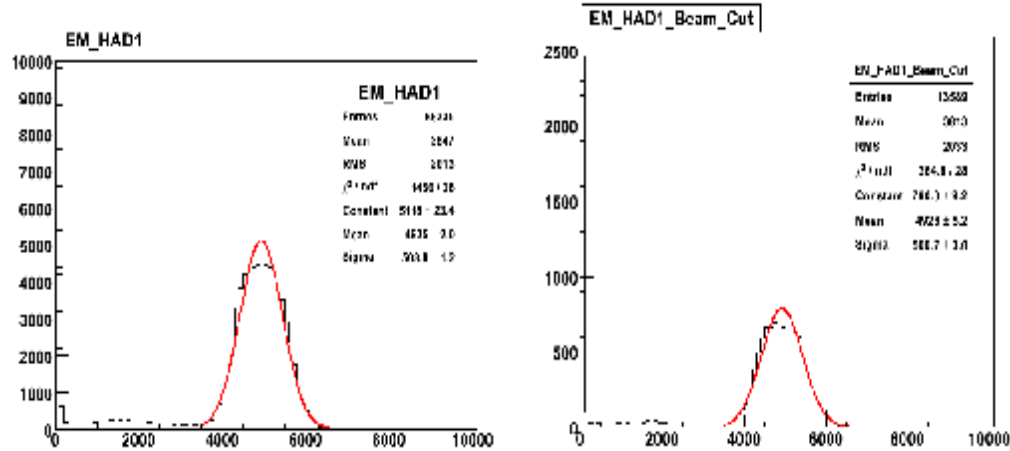
Figure 4.24. Signal distribution of the sum of the signals in EM1, EM3 and HAD1 channels, fitted by a Gaussian distribution, before (left) and after (right) a 1cm × 1cm spatial cut of the beam profile.

The signal amplitudes were found to be symmetric and well fitted by a Gaussian function after applying the spatial cut to the beam profile. Figure 4.25 shows the peak position as a function of the beam energy, illustrating the linear response of the calorimeter in the explored energy range. The average signal amplitude, expressed in units of fC or ADC counts, is satisfactorily fitted by the formula:

Average signal amplitude in ADC count $= a + b \times E$ (4.1)

where the energy E is in GeV. The fitted values of the parameters for each configuration are shown in the insets of each plot in Figure 4.25.
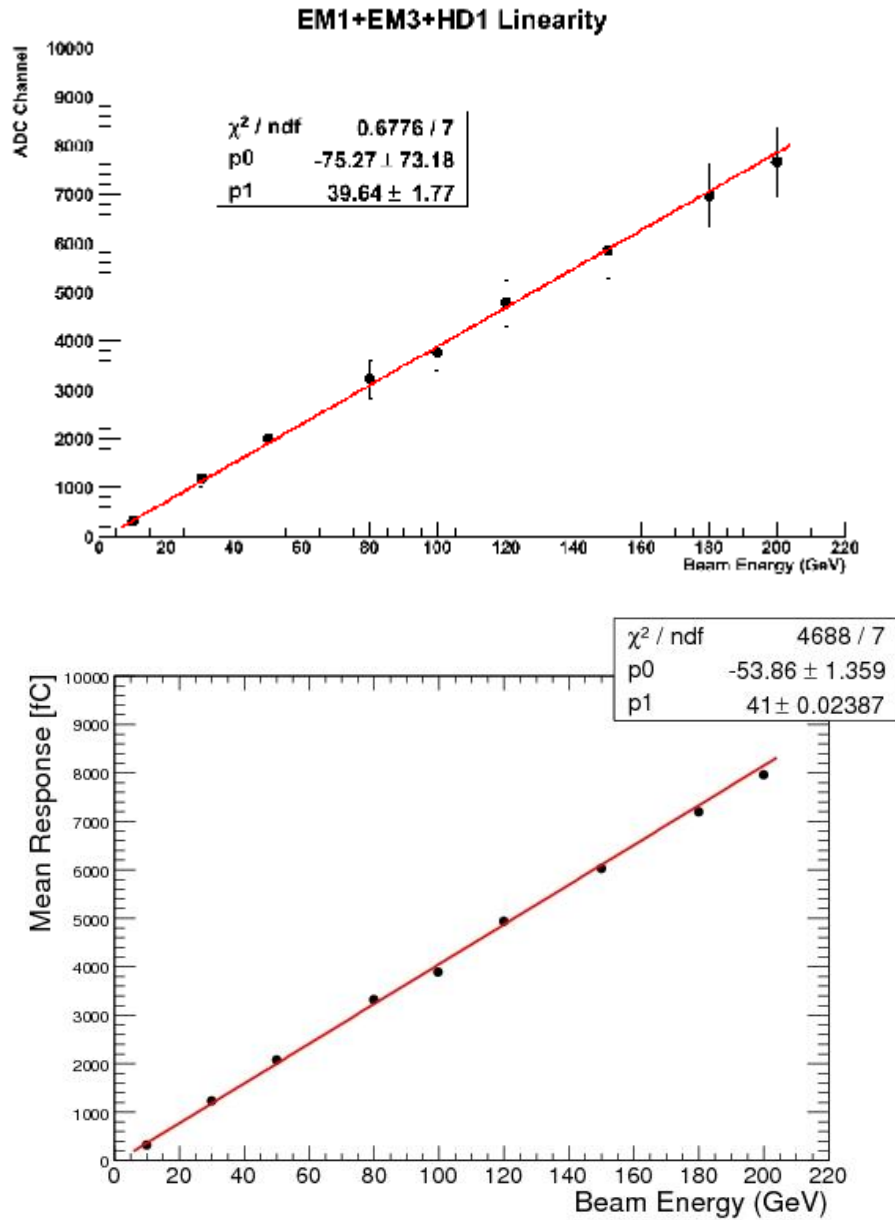
Figure 4.25. Energy linearity of CASTOR Prototype III using stand-alone libraries (HTBDAQ) (upper) (CASTOR EDR, 2007). Energy linearity of Prototype III using CMS Software (CMSSW and HCAL-DQM Module) (bottom) (Basegmez et al., 2008).

### 4.3.3. Energy Leakage and Beam Contamination from Hadronic Particles

Electrons of high energy are likely to deposit part of their energy in the first hadronic channels of the calorimeter, hence the energy "leakage" of electrons in the hadronic section was studied. Figure 4.26 shows the total electromagnetic energy with respect to the energy in the first hadronic channel, for electron beams of $E = 50$ and $E = 200$ GeV. The inter-calibration constants were applied for summing the signals. The feature at low energy in EM total energy vs. HD1 is from pion contamination in the electron beam.
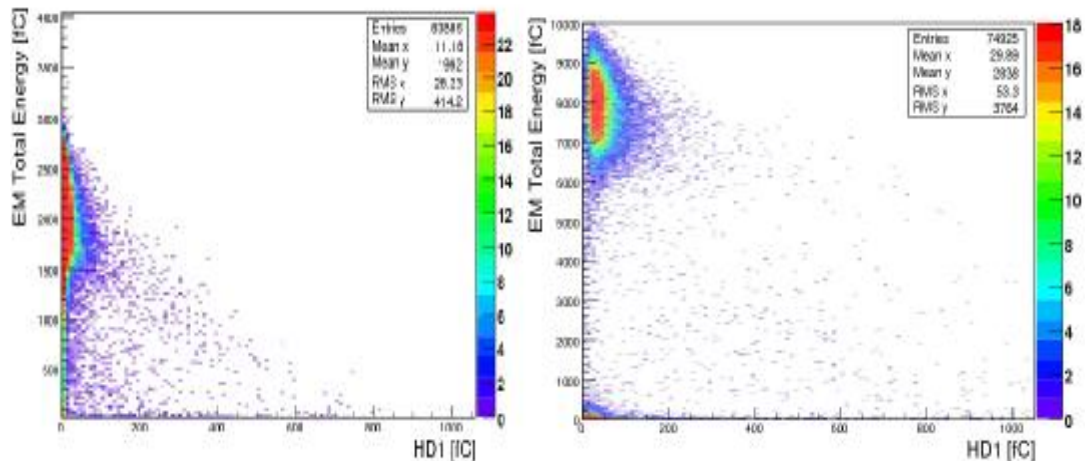
Figure 4.26. The sum of the signal in the EM section EM1, EM3 versus the signal in the first hadronic section of the CASTOR prototype III, for electron beams of $E = 50$ GeV (left) and $E = 200$ GeV (right) (Aslanoglou et al., 2008).

The events with very low EM energy were associated with contamination of the beam with pions, which could be finally filtered out by imposing a cut to the measured signal in the hadronic channels of the calorimeter (e.g. *E<10* or *E < 20* fC). The extended tails which were observed in the electrons spectra were thus removed, as can be seen in Figure 4.27, for an electron beam of $E = 120$ GeV. Figure 4.28 shows another example, for the 150 GeV electron beam.
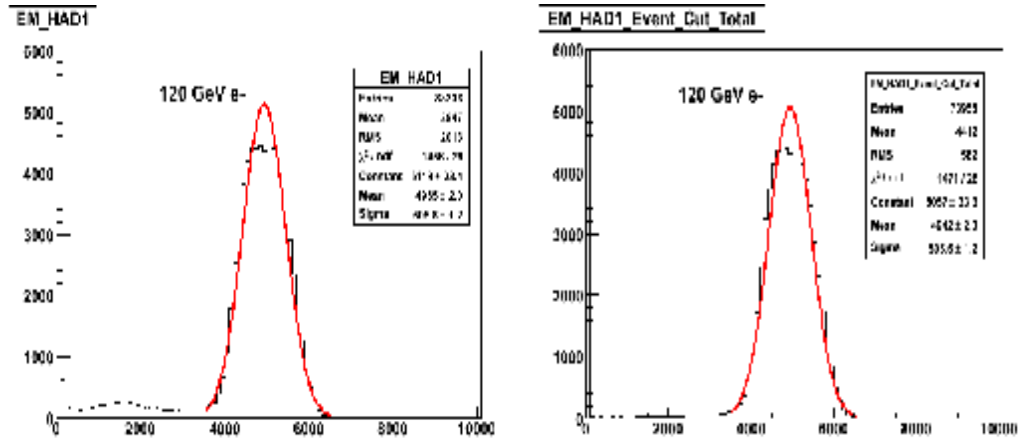
Figure 4.27. Electron signal peak for the 120 GeV beam. The raw signal distribution exhibits extended tails in the low energy region which were cleared away after a cut to the signal in the hadronic channels.
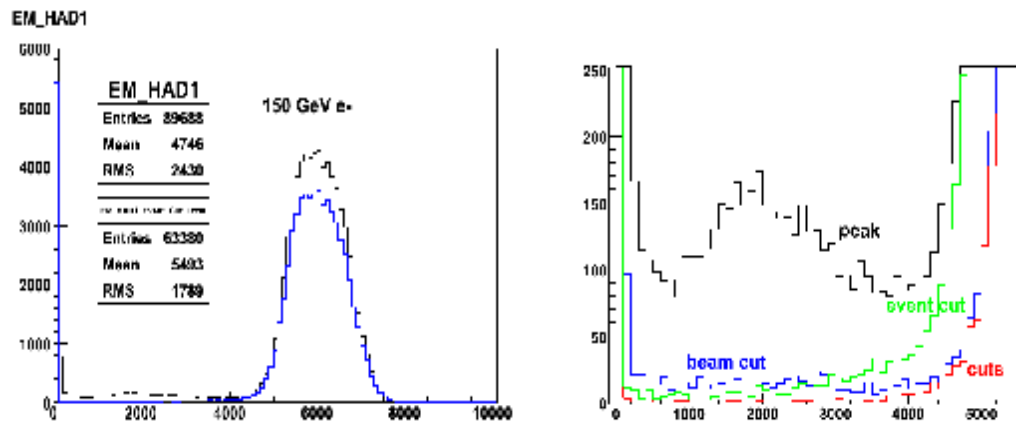
Figure 4.28. Left: Electron signal peak for the 150 GeV beam, without any cut (black) and after applying a cut to the hadronic channels of the prototype. Right: Zoomed view of the signal distribution for the low energy events without any cut (black) and after applying a) a cut to the hadronic channels (green), b) a spatial cut to the beam profile (blue) and c) both cuts (red).
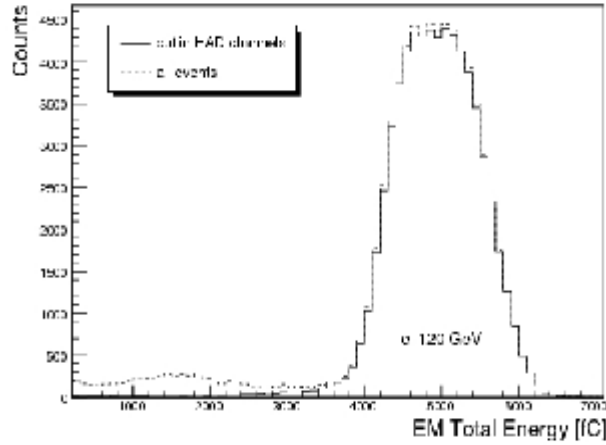
Figure 4.29. The signal distribution before and after 20 fC event cut.

The events which contributed to the low energy tails ("plato") were studied separately and it was found that the corresponding mean response per channel had similar variation to the signal produced by pion beams (see Figure 4.30), hence they were clearly associated with pion contamination. The Figure 4.29. shows this energy tails before and after event cut. It can be clearly seen from figure that after applying cut, the tail disappeared.
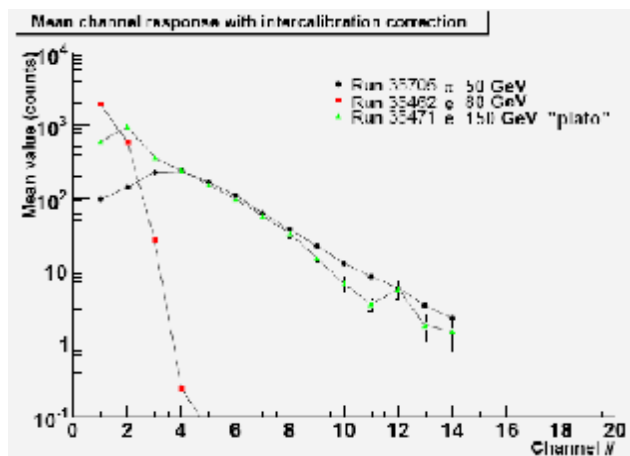

Figure 4.30. Mean signal per channel for $E = 80$, 150 GeV electrons and $E = 50$ GeV pions. For the 150 GeV electron beam, only the low energy events are considered and they exhibit similar variation to the signal produced by the 50 GeV pion beam (Aslanoglou et al., 2008).

4.3.4. Energy Resolution

The relative energy resolution of the calorimeter was studied by plotting the normalized width of the Gaussian signal amplitudes, *σ/E*, with respect to the incident beam electron energy, *E*(GeV) and fitting the data points with the functional forms (Aslanoglou et al., 2008):

$$\frac{\sigma}{E} = P_0 + \frac{P_1}{\sqrt{E}}$$

$$\text{(4.2)}$$

$$\frac{\sigma}{E} = P_0 \oplus \frac{P_1}{\sqrt{E}}$$

$$\text{(4.3)}$$

$$\frac{\sigma}{E} = P_0 \oplus \frac{P_1}{\sqrt{E}} \oplus \frac{P_2}{E}$$

$$\text{(4.4)}$$

Figures 4.31, 4.32 and 4.33 show the measured energy resolution for the case of the Hamamatsu PMTs. The measured stochastic term is 68-83 %, whereas the constant term is around 4-8%. The resolution of the calorimeter for energies above 150 GeV is below 10%.
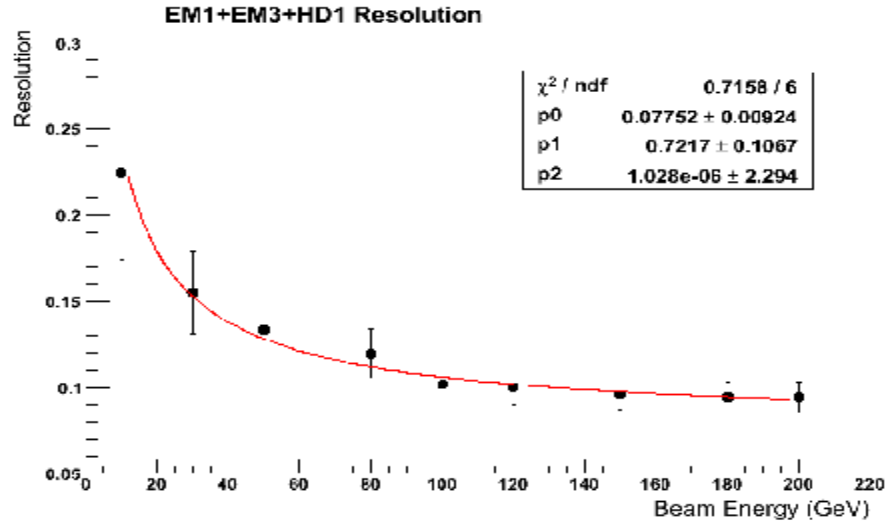
Figure 4.31. Energy resolution of calorimeter using stand-alone libraries (HTBDAQ) (CASTOR EDR, 2007). The data points are fitted the equation (4.4) with 3 parameters.
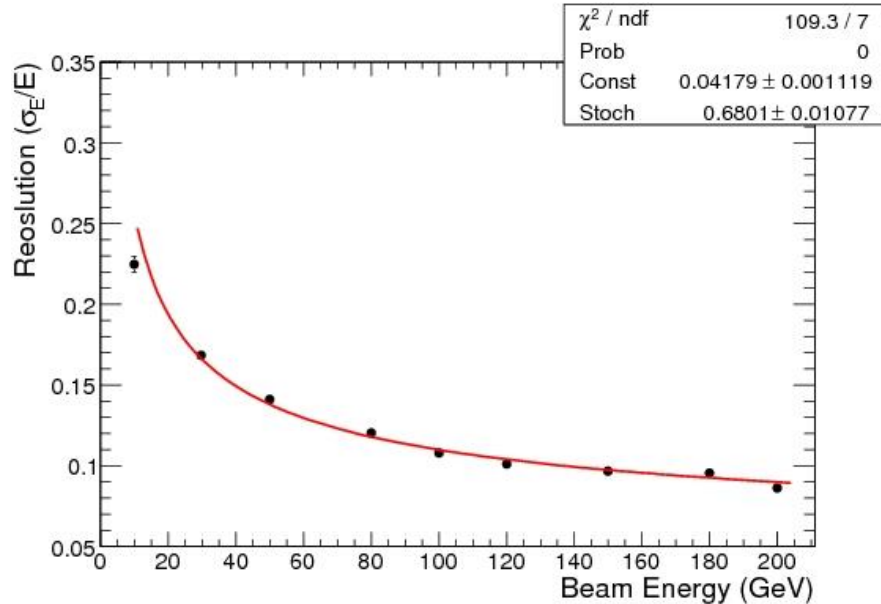

Figure 4.32. Energy resolution of prototype III. The data points are fitted with equation (4.3) (Basegmez et al., 2008).
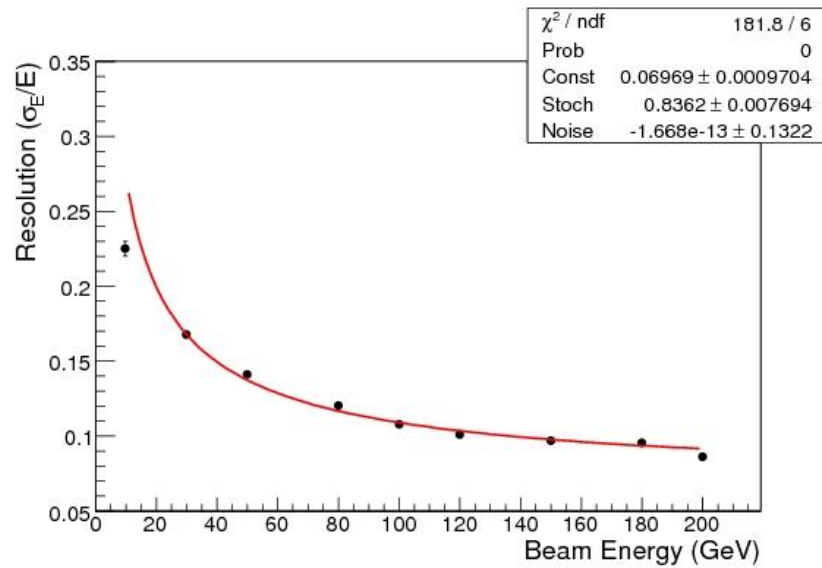
Figure 4.33. Energy resolution of prototype III. The data points are fitted with equation (4.4) (Basegmez et al., 2008).

5. DISCUSSION AND CONCLUSION

The CASTOR forward calorimeter will significantly enhance the pseudorapidity range of the CMS experiment, providing useful energy measurements in the very forward region. With a broad physics program, both for proton-proton and lead-lead collisions, CASTOR will contribute mainly to the study of exotic events in heavy-ions, in search of Centauro-type events and strangelets, as well as low-x QCD and diffractive physics. Consisting of successive layers of tungsten and quartz plates, one of the novel characteristics of CASTOR calorimeter, due to its detailed longitudinal segmentation, is the ability to read out the signal along the longitudinal direction of the electromagnetic and hadronic showers.

The performance studies of the final prototype of CASTOR calorimeter were performed with the data which were collected during the test beam of 2007 at the H2 CERN/SPS beam line. The analysis was performed using the CMSSW framework, as well as a standalone HCAL library. The results presented in this thesis, focus on the EM section of the prototype, and include studies for the energy response. It is shown that the prototype exhibits good energy linearity, while the energy resolution is characterized by a stochastic term of (68-83)% and a constant term (4-8)%. The results are summarized in Table 5.1. For relatively high energies, above 150 GeV, the energy resolution of the calorimeter was found to be less than 10%. The measured performance of the prototype, should be sufficient to meet the physics goal of the detector.

Table 5.1. Energy resolution fit parameters obtained.

Fit formula	p_0	p_1	p_2	x^2/ndf
(4.3)	0.042 ± 0.001	0.68 ± 0.01	-	109.3/7
(4.4)	0.007 ± 0.001	0.84 ± 0.077	$\sim -1.7e\text{-}13$	181.8/6

For the analysis, a spatial cut on the profile was applied, using the ADC information of the downstream wire chambers, as well as cuts in the hadronic channels of the prototype which made possible the study of the pion contamination of the beam. It was found that considerable amount of muon contaminates the electron beam. After the cut on the beam profile, the electron peaks were found to be significantly improved and well fitted by Gaussian distributions. For the summation of the energy in multiple channels of the prototype, the inter-calibration constants were used. They were calculated from the muon peaks, which were clearly separated from the pedestal. Information from other beam line detectors, not used for the purposes of the present thesis, could further improve the quality of the data and results.

Due to the different characteristics of the final prototype III, with respect to the first two prototypes tested in previous beam tests, no direct comparison can be easily made between the different studies due to the fact that each prototype has been tested for different purposes. The dimensions of the tungsten and quartz plates, as well as the geometry of the light-guides, were not identical, hence the performance of the prototypes cannot be compared in absolute values but we can say that each component of prototype III was working properly and the calorimeter prototype III determined the final design for the CASTOR calorimeter.

REFERENCES

AFFOLDER, T., et al., for the CDF collaboration, "Charged jet evolution and the underlying event in proton-antiproton collisions at 1.8 TeV", Phys. Rev. D, Vol. 65, 09-2002

ANGELIS, A.L.S. and PANAGIOTOU, A.D., 1997, CASTOR: A dedicated detector for the detection of centauros and strangelets at the LHC J. Phys. G: Nucl. Part. Phys. 23 (1997) 2069–2080.

ARNEDO, M. and DIEHL, M., 2005, arXiv:hep-ph/0511047 (2005)

ASAI, S., et al., Eur.Phys.J. C32S2 (2004) 19-54

ASLANOGLOU et al., 2006, First performance studies of a prototype for the CASTOR forward calorimeter at the CMS experiment, CMS-NOTE 2006-142.

ASLONLOGLOU et al., 2007, Performance Studies of Prototype II for the CASTOR forward Calorimeter at the CMS Experiment, arXiv:0706.2641v2 [physics.ins-det].

ASLANOGLOU et al., 2008, Performance studies of the final prototype for the CASTOR forward calorimeter at the CMS experiment CMS NOTE 2008/- (in preparation)

BASEGMEZ et al., 2008, Performance studies of the prototype III of CASTOR forward calorimeter at the CMS experiment, Presented at the Poster Session of the Quark Matter 2008 Conference, Jaipur, India, CMS-CR 2008/039

CASTOR Engineering Design Report, 2007, CERN, https://twiki.cern.ch/twiki/bin/view/CMS/CastorEDR

CMS Physics Technical Design Report, 2007, Vol II, CERN

D'ENTERRIA, D., Low-x QCD with CMS at the LHC, 2007, The European Physical Jurnal C Eur. Phys. J. C 49, 155–162 (2007) The European Physical Journal C DOI 10.1140/epjc/s10052-006-0078-5

D'ENTERRIA, D.Forward Physics at the LHC, 2007, XV Workshop on Deep-Inelastic Scattering and Related Topics talk, Munich

D'ENTERRIA, D., 2007, CASTOR Physics, Beam-Tests Results and Calibration, CASTOR Engineering Design Review talk, CERN

D' ENTERRIA, D., et al. and the CMS collaboration, 2007, J. Phys. G: Nucl. Part. Phys. 34 (2007) 2307–2455

D' ENTERRIA, D., 2008, Forward physics at the LHC: QCD, electroweak & Higgs, QCD- School Les Houches talk, March 25th - Apr. 4th, 2008

FABJAN, C.W. and GIANOTTI, F., 2003, Calorimetry for Particle Physics, CERN-EP/2003-075, CERN

GLADYSZ-DZIADUS, E., for the CASTOR group, 2002, CASTOR: Centauro And Strange Object Research in nucleus-nucleus collisions at LHC, arXiv:hep-ex/0209008v2

HEAVY ION PHYSICS TDR, 2007 Addendum I, (ed) D'Enterria, D. On behalf of the CMS Collaboration,

LEO, W.R., 1994.Techniques for Nuclear and Particle Physics Experiments, New York

MAVROMANOLAKIS, G., 2003. Quartz fiber calorimetry and calorimeters, Cambridge, UK

MUELLER A.H. and NAVALET, H., Nucl. Phys. B 282 (1987) 727

PANAGIOTOU,A.P.,2007, CASTOR EDR approval talk, CERN

PANAGIOTOU, A.D and KATSAS, P., 2006, Search for Strange Quark Matter with the CMS/CASTOR detector at the LHC, Nuclear Physics A10674 (2006)

PARTICLE DATA GROUP, The Review of Particle Physics, http://pdg.lbl.gov/

VIRDEE, T.S., 1998, Calorimetry. CMS Collaboration,CERN, Geneva, CMS Conference Report,CMS-CR, 1998/026

WIGMANS, R., 2000. Calorimetry Energy Measurement in Particle Physics, Oxford University Press, UK, 17,726.

CURRICULUM VITAE

I was born in Dicle. I graduated from primary and secondary school in Adana. I completed my secondary school studies at Dervisler Ilkogretim Okulu. After that, I enrolled to the high school of Adana Kiz Lisesi and graduated. I enrolled to the Physics Department in Çukurova University and I graduated in 2005. After my bachelor degree, I continued to study for my Master in High Energy Physics, at the Institute of Natural and Applied Sciences in Çukurova University where I am still enrolled.